

# A Stable and High-Order Accurate Discontinuous Galerkin Based Splitting Method for the Incompressible Navier-Stokes Equations

Marian Piatkowski\*, Steffen Müthing, Peter Bastian<sup>a</sup>,

<sup>a</sup>*Interdisciplinary Center for Scientific Computing, Heidelberg University, D-69120 Heidelberg*

---

## Abstract

In this paper we consider discontinuous Galerkin (DG) methods for the incompressible Navier-Stokes equations in the framework of projection methods. In particular we employ symmetric interior penalty DG methods within the second-order rotational incremental pressure correction scheme. The major focus of the paper is threefold: i) We propose a modified upwind scheme based on the Vijayasundaram numerical flux that has favourable properties in the context of DG. ii) We present a novel postprocessing technique in the Helmholtz projection step based on  $H(\text{div})$  reconstruction of the pressure correction that is computed locally, is a projection in the discrete setting and ensures that the projected velocity satisfies the discrete continuity equation exactly. As a consequence it also provides local mass conservation of the projected velocity. iii) Numerical results demonstrate the properties of the scheme for different polynomial degrees applied to two-dimensional problems with known solution as well as large-scale three-dimensional problems. In particular we address second-order convergence in time of the splitting scheme as well as its long-time stability.

*Keywords:* Navier-Stokes equations, High-order discontinuous Galerkin, Projection Methods, Incompressibility

---

## 1. Introduction

The application of discontinuous Galerkin (DG) methods to the Navier-Stokes equations is popular due to their potentially high order of convergence, the inf-sup stability and local mass conservation property [1, 2, 3]. The latter is generally not fulfilled for conforming finite element discretizations. In addition to the  $2 \times 2$  block structure arising from the saddle point system discontinuous Galerkin methods offer a further block structure when the unknowns associated with one cell of the mesh are grouped together. This data structure is essential for high-performance implementations of the discontinuous Galerkin method [4, 5] as it avoids costly memory gather and scatter operations when compared to conforming finite element methods.

Operator splitting methods for solving the stationary Navier-Stokes equations has been subject to detailed investigations for the recent decades. One possibility in the splitting methods is to split between the convective term and the saddle point structure which is realized in Glowinski's  $\Theta$ -scheme, [6, 7]. Another possibility is to split between incompressibility and dynamics which has been independently developed by Chorin [8] and Témam [9] and is referred to as Chorin's projection method. The latter splitting schemes have the appealing feature that at each time step, instead of solving a saddle point system, one only has to solve a vector-valued heat equation for the velocity (in the Stokes case) and a Poisson equation for the pressure. The choice of artificial boundary conditions on the pressure Poisson equation is a delicate issue in projection methods of this class [10, 11, 12]. Several higher-order extensions of Chorin's first order method

---

\*Corresponding author

*Email addresses:* marian.piatkowski@iwr.uni-heidelberg.de (Marian Piatkowski),  
steffen.muething@iwr.uni-heidelberg.de (Steffen Müthing), peter.bastian@iwr.uni-heidelberg.de (Peter Bastian)

have been suggested in the literature [13, 14, 15, 16, 17, 18]. Here we concentrate on the classic incremental pressure-correction scheme (IPCS) [19] and the rotational incremental pressure-correction scheme (RIPCS) [14].

The use of a DG spatial discretization within splitting schemes is a current subject of active research. A naive computation of the divergence free velocity by subtraction of the rotation free part is reported to be unstable when the spatial mesh is coarse and the time step is small, see [20, 21, 4], where several local postprocessing techniques are discussed to overcome this difficulty. In this paper we propose a new postprocessing technique based on  $H(\text{div})$  reconstruction of the discrete pressure gradient which is popular in porous media flow computations [22, 23]. The new approach provides a discrete velocity that satisfies the discrete continuity equation exactly and in consequence is locally mass conservative and defines a projection. These properties are not satisfied by the postprocessing schemes available in the literature.

The structure of the paper is organized as follows: in section 2 we recapitulate the discontinuous Galerkin discretization by the interior penalty method as presented in [2, 1]. In section 3 we discuss the Helmholtz decomposition, prove our main result and present the projection methods. In section 4 we elaborate on numerical experiments for the discontinuous Galerkin discretization based on the reference problems by [15, 16, 24, 18] and assess the properties of the new postprocessing scheme.

## 2. Discontinuous Galerkin discretization of the incompressible Navier-Stokes equations

In this section we present the spatial discretization of the Navier-Stokes system with an interior penalty DG method taken from [2]. The convective term is discretized using the Vijayasundaram flux.

The instationary incompressible Navier-Stokes equations in an open and bounded domain  $\Omega \subset \mathbb{R}^d$  ( $d = 2, 3$ ) determining the velocity  $v$  and pressure  $p$  for a right-hand side  $f$ , viscosity  $\mu$  and density  $\rho$  are given by

$$\rho \partial_t v - \mu \Delta v + \rho(v \cdot \nabla)v + \nabla p = f \quad \text{in } \Omega \times (0, T] \quad (1a)$$

$$\nabla \cdot v = 0 \quad \text{in } \Omega \times (0, T] \quad (1b)$$

$$v = v_0 \quad \text{for } t = 0 \quad (1c)$$

and either Dirichlet boundary conditions:

$$v = g \quad \text{on } \Gamma_D = \partial\Omega, t \in (0, T] \quad (1d)$$

$$\int_{\Omega} p dx = 0 \quad \text{for all } t \in (0, T] \quad (1e)$$

or mixed boundary conditions:

$$v = g \quad \text{on } \Gamma_D \neq \{\partial\Omega, \emptyset\} \quad (1f)$$

$$\mu \nabla v n - p n = 0 \quad \text{on } \Gamma_N = \partial\Omega \setminus \Gamma_D \quad (1g)$$

with  $(0, T]$  being the time interval of interest. For pure Dirichlet boundary conditions  $g$  is required to satisfy the compatibility condition  $\int_{\partial\Omega} g \cdot n dx = 0$ . In the numerical examples below we will also consider periodic boundary conditions in addition. Under appropriate assumptions the Navier-Stokes problem in weak form has a solution in  $(H^1(\Omega))^d \times L^2(\Omega)$  for  $t \in (0, T]$ , [25, 26]. In case of pure Dirichlet boundary conditions the pressure is only determined up to a constant and is in the space  $L_0^2(\Omega) = \{q \in L^2(\Omega) \mid \int_{\Omega} q dx = 0\}$ .

For the discretization let  $\mathcal{E}_h$  be an affine cubic mesh (the restriction to affine meshes is only needed when the Raviart-Thomas reconstruction is used) with maximum diameter  $h$ . We denote by  $\Gamma_h^{\text{int}}$  the set of all interior faces, by  $\Gamma_h^D$  the set of all faces intersecting with the Dirichlet boundary  $\Gamma_D$  and by  $\Gamma_h^N$  the set of all faces intersecting with the “do-nothing” boundary  $\Gamma_N$ . We set  $\Gamma_h = \Gamma_h^{\text{int}} \cup \Gamma_h^D \cup \Gamma_h^N$ . To an interior face  $e \in \Gamma_h^{\text{int}}$  shared by elements  $E_e^1$  and  $E_e^2$  we define an orientation through its unit normal vector  $n_e$  pointing

from  $E_e^1$  to  $E_e^2$ . The jump and average of a possibly vector-valued function  $\phi$  on a face is then defined by

$$\begin{aligned} [\phi] &= \phi|_{E_e^1} - \phi|_{E_e^2} = \phi^{\text{int}} - \phi^{\text{ext}}, \\ \{\phi\} &= \frac{1}{2}\phi|_{E_e^1} + \frac{1}{2}\phi|_{E_e^2} = \frac{1}{2}\phi^{\text{int}} + \frac{1}{2}\phi^{\text{ext}}. \end{aligned} \quad (2)$$

If  $e \in \partial\Omega$  then  $n_e$  corresponds to the outer normal vector  $n$ . Note that the definition of jump and average applies to scalar as well as vector-valued functions. An important property of jump and average is

$$[uv] = [u]\{v\} + \{u\}[v]. \quad (3)$$

Below we make heavy use of the notation

$$\begin{aligned} (u, v)_{0, \omega} &= \int_{\omega} uv \, dx, & (u, v \text{ scalar-valued}) \\ (u, v)_{0, \omega} &= \int_{\omega} u \cdot v \, dx, & (u, v \text{ vector-valued}) \\ (u, v)_{0, \omega} &= \int_{\omega} u : v \, dx, & (u, v \text{ matrix-valued}). \end{aligned}$$

The DG discretization on cuboid meshes is based on the non-conforming finite element space of polynomial degree  $p$

$$Q_h^p = \{v \in L^2(\Omega) \mid v|_E = q \circ \mu_E^{-1}, q \in \mathbb{Q}_{p,d}, E \in \mathcal{E}_h\} \quad (4)$$

where  $\mu_E : \hat{E} \rightarrow E$  is the transformation from the reference cube  $\hat{E}$  to  $E$  and  $\mathbb{Q}_{p,d}$  is the set of polynomials of maximum degree  $p$  in  $d$  variables. The approximation spaces for velocity and pressure are then

$$\mathbf{X}_h^p \times M_h^{p-1} = (Q_h^p)^d \times (Q_h^{p-1} \cap L_0^2(\Omega)) \quad (\text{Dirichlet b. c.}), \quad (5a)$$

$$\mathbf{X}_h^p \times M_h^{p-1} = (Q_h^p)^d \times Q_h^{p-1} \quad (\text{mixed b. c.}). \quad (5b)$$

We make use of the following mesh-dependent forms defined on  $\mathbf{X}_h^p \times \mathbf{X}_h^p$ ,  $\mathbf{X}_h^p \times M_h^{p-1}$  and  $M_h^{p-1}$ , respectively:

$$a(u, v) = d(u, v) + J_0(u, v), \text{ where} \quad (6a)$$

$$d(u, v) = \sum_{E \in \mathcal{E}_h} (\nabla u, \nabla v)_{0,E} - \sum_{e \in \Gamma_h^{\text{int}}} (\{\nabla u\} n_e, [v])_{0,e} - \sum_{e \in \Gamma_h^D} (\nabla u^{\text{int}} n_e, v^{\text{int}})_{0,e}, \quad (6b)$$

$$\begin{aligned} J_0(u, v) &= \epsilon \sum_{e \in \Gamma_h^{\text{int}}} (\{\nabla v\} n_e, [u])_{0,e} + \epsilon \sum_{e \in \Gamma_h^D} (\nabla v^{\text{int}} n_e, u^{\text{int}})_{0,e} \\ &\quad + \sum_{e \in \Gamma_h^{\text{int}}} \frac{\sigma}{h_e} ([u], [v])_{0,e} + \sum_{e \in \Gamma_h^D} \frac{\sigma}{h_e} (u^{\text{int}}, v^{\text{int}})_{0,e}, \end{aligned} \quad (6c)$$

$$b(v, q) = - \sum_{E \in \mathcal{E}_h} (\nabla \cdot v, q)_{0,E} + \sum_{e \in \Gamma_h^{\text{int}}} ([v] \cdot n_e, \{q\})_{0,e} + \sum_{e \in \Gamma_h^D} (v^{\text{int}} \cdot n, q^{\text{int}})_{0,e}, \quad (6d)$$

$$l(v; t) = \sum_{E \in \mathcal{E}_h} (f(t), v)_{0,E} + \epsilon \sum_{e \in \Gamma_h^D} (\nabla v^{\text{int}} n_e, g(t))_{0,e} + \sum_{e \in \Gamma_D} \frac{\sigma}{h_e} (g(t), v^{\text{int}})_{0,e}, \quad (6e)$$

$$r(q; t) = \sum_{e \in \Gamma_h^D} (g(t) \cdot n, q^{\text{int}})_{0,e}. \quad (6f)$$

Here we made the time dependence of the right hand side functionals explicit. For ease of writing this will be omitted mostly below. In the interior penalty parameter  $\sigma/h_e$ , the denominator accounts for the mesh dependence. The formula for  $h_e$ ,

$$h_e = \begin{cases} \frac{\min(|E^{\text{int}}(e)|, |E^{\text{ext}}(e)|)}{|e|} & , E^{\text{int}}(e) \cap E^{\text{ext}}(e) = e \\ \frac{|E^{\text{int}}(e)|}{|e|} & , E^{\text{int}}(e) \cap \Gamma_D = e \end{cases},$$

has been stated in [27] and it was proven that this choice ensures coercivity of the bilinear form for anisotropic meshes. For  $\sigma$  we choose  $\sigma = \alpha p(p + d - 1)$  as in [28] with  $\alpha$  a user-defined parameter. In  $J_0$  the *Symmetric Interior Penalty Galerkin (SIPG)* ( $\epsilon = -1$ ) method is preferred since the matrix of the linear system in absence of the convection term is then symmetric. Other choices are the NIPG ( $\epsilon = 1$ ) or IIPG ( $\epsilon = 0$ ) method.

The nonlinear term in the Navier-Stokes equations can either be treated with the standard (centered) discretization,

$$c(u; z, \theta) = \sum_{E \in \mathcal{E}_h} ((u \cdot \nabla) z, \theta)_{0,E}, \quad (7)$$

or by an upwind discretization as presented below in section 2.1.

The discrete in space, continuous in time formulation of the Navier-Stokes problem (1) now seeks to find  $v_h(t) : (0, T] \rightarrow \mathbf{X}_h^p$ ,  $p_h(t) : (0, T] \rightarrow M_h^{p-1}$ :

$$\rho(\partial_t v_h, \varphi)_{0,\Omega} + \mu a(v_h, \varphi) + \rho c(v_h; v_h, \varphi) + b(\varphi, p_h) = l(\varphi), \quad (8a)$$

$$b(v_h, q) = r(q), \quad (8b)$$

for all  $(\varphi, q) \in \mathbf{X}_h^p \times M_h^{p-1}$ . The following observation will be used in several circumstances below.

**Observation 1.** The bilinear form  $b(v, q)$  has the equivalent representation

$$b(v, q) = \sum_{E \in \mathcal{E}_h} (v, \nabla q)_{0,E} - \sum_{e \in \Gamma_h^{\text{int}}} (\{v\} \cdot n_e, [q])_{0,e} - \sum_{e \in \Gamma_h^N} (v \cdot n_e, q)_{0,e}. \quad (9)$$

This holds true for Dirichlet and mixed boundary conditions (in the latter case just set  $\Gamma_h^N = \emptyset$ ).

*Proof.* Follows from integration by parts and (3):

$$\begin{aligned} b(v, q) &= - \sum_{E \in \mathcal{E}_h} (\nabla \cdot v, q)_{0,E} + \sum_{e \in \Gamma_h^{\text{int}}} ([v] \cdot n_e, \{q\})_{0,e} + \sum_{e \in \Gamma_h^D} (v \cdot n_e, q)_{0,e} \\ &= \sum_{E \in \mathcal{E}_h} [(v, \nabla q)_{0,E} - (v \cdot n_E, q)_{0,\partial E}] + \sum_{e \in \Gamma_h^{\text{int}}} ([v] \cdot n_e, \{q\})_{0,e} + \sum_{e \in \Gamma_h^D} (v \cdot n_e, q)_{0,e} \\ &= \sum_{E \in \mathcal{E}_h} (v, \nabla q)_{0,E} + \sum_{e \in \Gamma_h^D} [(v \cdot n_e, q)_{0,e} - (v \cdot n_e, q)_{0,e}] - \sum_{e \in \Gamma_h^N} (v \cdot n_e, q)_{0,e} \\ &\quad + \sum_{e \in \Gamma_h^{\text{int}}} [([v] \cdot n_e, \{q\})_{0,e} - ([v] \cdot n_e, \{q\})_{0,e} - (\{v\} \cdot n_e, [q])_{0,e}] \\ &= \sum_{E \in \mathcal{E}_h} (v, \nabla q)_{0,E} - \sum_{e \in \Gamma_h^{\text{int}}} (\{v\} \cdot n_e, [q])_{0,e} - \sum_{e \in \Gamma_h^N} (v \cdot n_e, q)_{0,e}. \end{aligned} \quad (10)$$

□

As a corollary we obtain the following local mass conservation property by testing (8b) with  $q = \chi_E$ , the characteristic function of element  $E$ , and using Observation 1:

$$\sum_{e \in \Gamma_h^{\text{int}}, e \in \partial E} (\{v\} \cdot n_e, 1)_{0,e} + \sum_{e \in \Gamma_h^N, e \in \partial E} (v \cdot n_e, 1)_{0,e} + \sum_{e \in \Gamma_h^D, e \in \partial E} (g \cdot n, 1)_{0,e} = 0. \quad (11)$$

### 2.1. Discretization of the convective part

For higher Reynolds numbers we employ a suitable upwind discretization based on the Vijayasundaram numerical flux adapted from DG methods for inviscid compressible flow [29, 30].

Note that due to  $\nabla \cdot v = 0$  the convective term in the momentum equations can be written equivalently as  $(v \cdot \nabla)v = \nabla \cdot (v \otimes v)$  where

$$F(v) = v \otimes v = [v_1 v, \dots, v_d v] = [F_1(v), \dots, F_d(v)]$$

is the convective flux matrix with columns  $F_k(v) = v_k v$  and  $\nabla F_k(v) = (v_k I + v \otimes e_k)$ .  $I$  denotes the identity matrix and  $(e_k)_i = \delta_{ik}$  are the coordinate unit vectors. In order to derive the upwinding we consider the first order system

$$\partial_t v + \nabla \cdot F(v) = 0$$

which is said to be hyperbolic if the matrix

$$P(v, n) = \sum_{k=1}^d n_k \nabla F_k(v) = (v \cdot n)I + v \otimes n$$

is real diagonalizable for all  $v, n \in \mathbb{R}^d$  with  $\|n\| = 1$  [31]. This is indeed the case for  $v \cdot n \neq 0$ . When  $v \cdot n = 0$ ,  $P(v, n) = v \otimes n$  has  $d$  eigenvalues zero with a corresponding eigenspace  $W_n^\perp = \{w : w \cdot n = 0\}$  of dimension  $d - 1$ .

When discretizing the conservative form of the convective terms with DG one uses element-wise integration by parts to arrive at

$$\begin{aligned} c(v; v, \varphi) &= (\nabla \cdot F(v), \varphi)_{0, \Omega} = \sum_{E \in \mathcal{E}_h} (\nabla \cdot F(v), \varphi)_{0, E} = - \sum_{E \in \mathcal{E}_h} (F(v), \nabla \varphi)_{0, E} + \sum_{E \in \mathcal{E}_h} (F(v)n, \varphi)_{0, \partial E} \\ &= - \sum_{E \in \mathcal{E}_h} (F(v), \nabla \varphi)_{0, E} + \sum_{e \in \Gamma_h^{\text{int}}} ([F(v)n_e \cdot \varphi], 1)_{0, e} + \sum_{e \in \Gamma_h^P \cup \Gamma_h^N} (F(v)n, \varphi)_{0, e} \end{aligned}$$

Now the flux in face normal direction  $F(v)n_e$  needs to be replaced by a *consistent* and *conservative* numerical flux function  $\hat{F}(v, n_e)$  which we now derive. Since  $F_k(v) = v_k v$  is homogeneous of degree 2 it admits a representation

$$F_k(v) = \frac{1}{2} \nabla F_k(v) v$$

and therefore

$$F(v)n = \frac{1}{2} P(v, n)v = \frac{1}{2} [(v \cdot n)I + v \otimes n]v = B_{\frac{1}{2}}(v)v.$$

Using the identity  $(v \cdot n)v = (v \otimes n)v$  we see

$$F(v)n = B_\beta(v)v = [(1 - \beta)(v \cdot n) + \beta v \otimes n]v$$

For  $v \cdot n \neq 0$ ,  $B_\beta(v, n)$  is real diagonalizable with eigenvalues  $\lambda_{\beta, i} \in \mathbb{R}$  and a full set of right eigenvectors  $r_i$ ,  $\text{span}\{r_1, \dots, r_{d-1}\} = W_n^\perp$ ,  $r_d = v$ , admitting the decomposition

$$B_\beta(v, n) = B_\beta^+(v, n) + B_\beta^-(v, n),$$

where  $B_\beta^\pm(v, n) = P D_\beta^\pm P^{-1}$ ,  $P = [r_1, \dots, r_d]$ ,  $D_\beta^\pm$  diagonal matrices with  $(D_\beta^+)_{ii} = \max(0, \lambda_{\beta, i})$  and  $(D_\beta^-)_{ii} = \min(0, \lambda_{\beta, i})$  (all eigenvectors and eigenvalues depending on  $v$  and  $n$ ).

Following [30], in the DG scheme we employ the *Vijayasundaram* numerical flux given by

$$\hat{F}_\beta(v, n_e) = B_\beta^+(\{v\}, n_e)v^{\text{int}} + B_\beta^-(\{v\}, n_e)v^{\text{ext}}. \quad (12)$$

Here the the matrices  $B_\beta^\pm(\{v\}, n_e)$  are *not* applied to  $\{v\}$  and therefore  $(\{v\} \cdot n)I$  and  $\{v\} \otimes n$  act differently. The effect is shown by the following

**Observation 2.** Assume  $\{v\} \cdot n \neq 0$ . Then the numerical flux (12) satisfies

$$\begin{aligned}\hat{F}_\beta(v, n_e) &= (1 - \beta) [\max(0, \{v\} \cdot n_e) v^{\text{int}} + \min(0, \{v\} \cdot n_e) v^{\text{ext}}] \\ &\quad + \beta [H(\{v\} \cdot n_e) (v^{\text{int}} \cdot n_e) + H(-\{v\} \cdot n_e) (v^{\text{ext}} \cdot n_e)] \{v\}.\end{aligned}$$

where  $H(x)$  is the Heaviside function.

*Proof.* We consider the inside part. The eigenvectors of  $B_\beta(\{v\}, n_e)$  are  $d - 1$  vectors spanning  $W_n^\perp$  and  $\{v\}$  independent of  $\beta \in [0, 1]$ . We can uniquely decompose

$$v^{\text{int}} = w + \alpha \{v\} = \left( v^{\text{int}} - \frac{v^{\text{int}} \cdot n_e}{\{v\} \cdot n_e} \{v\} \right) + \frac{v^{\text{int}} \cdot n_e}{\{v\} \cdot n_e} \{v\}$$

where  $w \in W_n^\perp$ . Now

$$\begin{aligned}B_\beta^+(\{v\}, n_e) v^{\text{int}} &= B_\beta^+(\{v\}, n_e) (w + \alpha \{v\}) \\ &= (1 - \beta) \max(0, \{v\} \cdot n_e) w + \max(0, \{v\} \cdot n_e) \alpha \{v\} \\ &= \max(0, \{v\} \cdot n_e) v^{\text{int}} - \beta \max(0, \{v\} \cdot n_e) w \\ &= \max(0, \{v\} \cdot n_e) v^{\text{int}} - \beta \max(0, \{v\} \cdot n_e) \left( v^{\text{int}} - \frac{v^{\text{int}} \cdot n_e}{\{v\} \cdot n_e} \{v\} \right) \\ &= (1 - \beta) \max(0, \{v\} \cdot n_e) v^{\text{int}} + \beta \frac{\max(0, \{v\} \cdot n_e) (v^{\text{int}} \cdot n_e)}{\{v\} \cdot n_e} \{v\}.\end{aligned}$$

$B_\beta^-(\{v\}, n_e) v^{\text{ext}}$  can be treated in the same way.  $\square$

The observation shows that for  $\beta > 0$  the  $v \otimes n_e$  part gives a contribution in the flux in the direction of  $\{v\}$ , i.e. a central flux which moreover might have the wrong sign since the signs of  $\{v\} \cdot n_e$  and  $v^{\text{int}} \cdot n$  or  $v^{\text{ext}} \cdot n$  might differ since the DG velocity is not in  $H(\text{div}; \Omega)$ . (Note, however, that the new projection scheme described below improves significantly on this point). Also note that the upwind decision is based on the average velocity which is locally mass conservative due to (11).

For these reasons we propose to employ  $\beta = 0$  in the numerical flux function, leading to the simple form:

$$\hat{F}_e(v, n_e) = \begin{cases} \max(0, \{v\} \cdot n_e) v^{\text{int}} + \min(0, \{v\} \cdot n_e) v^{\text{ext}} & e \in \Gamma_h^{\text{int}} \\ \max(0, v^{\text{int}} \cdot n_e) v^{\text{int}} + \min(0, v^{\text{int}} \cdot n_e) g & e \in \Gamma_h^D \\ \max(0, v^{\text{int}} \cdot n_e) v^{\text{int}} & e \in \Gamma_h^N \end{cases}$$

and the upwind DG discretization of the convective term

$$\hat{c}(v; v, \varphi) = - \sum_{E \in \mathcal{E}_h} (F(v), \nabla \varphi)_{0,E} + \sum_{e \in \Gamma_h^{\text{int}}} (\hat{F}_e(v, n_e), [\varphi])_{0,e} + \sum_{e \in \Gamma_h^D \cup \Gamma_h^N} (\hat{F}_e(v, n_e), \varphi)_{0,e}. \quad (13)$$

### 3. Projection methods

#### 3.1. Continuous Helmholtz decomposition

The Helmholtz decomposition takes a fundamental role in the construction of splitting methods for incompressible flows. It states that any vector field in  $L^2(\Omega)^d$  can be decomposed into a divergence-free contribution and an irrotational contribution, see e.g. [8, 17, 32, 33, 34]. In order to define the decomposition boundary conditions on the pressure need to be enforced which are not part of the underlying Navier-Stokes equations. The choice and consequence of these boundary conditions is a delicate issue in projection methods [10, 11, 12]. Before turning to the Helmholtz decomposition in the discrete setting of DG methods we recall the Helmholtz decomposition in the weak continuous setting.

First consider Dirichlet boundary conditions (1d), (1e). Let us denote the space of weakly divergence free functions by

$$H(\Omega) := \{v \in L^2(\Omega)^d \mid (v, \nabla f)_{0,\Omega} - (g \cdot n, f)_{0,\Gamma_D} = 0 \forall f \in H^1(\Omega)\} \quad (14)$$

where  $\Gamma_D = \partial\Omega$ . This definition is motivated by the identity  $(\nabla \cdot v, f)_{0,\Omega} = -(v, \nabla f)_{0,\Omega} + (g \cdot n, f)_{0,\Gamma_D} = 0$  which holds true for  $v \in H(\text{div}; \Omega) = \{u \in L^2(\Omega)^d \mid \nabla \cdot u \in L^2(\Omega)\}$ . In that case the normal component of  $v$  can be prescribed on the boundary. In addition, we employ the pressure space

$$\Psi_D(\Omega) := \{q \in H^1(\Omega) \mid (q, 1)_{0,\Omega} = 0\}. \quad (15)$$

in the following decomposition.

**Theorem 1** (Helmholtz decomposition, Dirichlet boundary conditions). For any  $w \in L^2(\Omega)^d$  there are unique functions  $v \in H(\Omega)$  and  $\psi \in \Psi_D(\Omega)$  such that

$$w = v + \nabla \psi.$$

*Proof.* Define  $\psi \in \Psi_D(\Omega)$  by

$$(\nabla \psi, \nabla q)_{0,\Omega} = (w, \nabla q)_{0,\Omega} - (g \cdot n, q)_{0,\Omega} \quad \forall q \in \Psi_D(\Omega). \quad (16)$$

According to the Lax-Milgram theorem this problem has a unique solution. Since any  $f \in H^1(\Omega)$  can be written as  $f = q + \text{const}$  with  $q \in \Psi_D(\Omega)$ , equation (16) holds also true for all test functions in  $H^1(\Omega)$  (Note the compatibility condition on  $g$ ). Now set  $v = w - \nabla \psi$  and verify that  $(v, \nabla f)_{0,\Omega} - (g \cdot n, f)_{0,\Gamma_D} = 0$  for all  $f \in H^1(\Omega)$ .  $\square$

**Remark 1.** 1) Note that equation (16) is the weak formulation of a Poisson equation with homogeneous Neumann boundary conditions.

2) The map  $\mathcal{P} : L^2(\Omega)^d \rightarrow H(\Omega)$  given by  $\mathcal{P}w = w - \nabla \psi$  is a projection since the right hand side of (16) is zero for  $w \in H(\Omega)$ .  $\mathcal{P}$  is called the *continuous Helmholtz projection*.

3) The construction above can be equivalently written as

$$(v, \varphi)_{0,\Omega} + (\nabla \psi, \varphi)_{0,\Omega} = (w, \varphi)_{0,\Omega} \quad \forall \varphi \in L^2(\Omega)^d \quad (17a)$$

$$(v, \nabla q)_{0,\Omega} = (g, q)_{0,\Gamma_D} \quad \forall q \in \Psi_D(\Omega) \quad (17b)$$

since from the first equation we get  $v = w - \nabla \psi$  and inserting in the second equation yields (16).

4) In Chorin's classical projection scheme [8] the (divergence-free) velocity  $v^{k+1}$  and pressure  $p^{k+1}$  at time  $t^{k+1}$  are computed from a tentative velocity  $w^{k+1}$  by the system

$$\begin{aligned} \frac{v^{k+1} - w^{k+1}}{\Delta t} + \nabla p^{k+1} &= 0 \\ \nabla \cdot v^{k+1} &= 0 \end{aligned}$$

in strong form. Setting  $\psi^{k+1} = \Delta t p^{k+1}$  this is equivalent to

$$\begin{aligned} v^{k+1} + \nabla \psi^{k+1} &= w^{k+1} \\ \nabla \cdot v^{k+1} &= 0 \end{aligned}$$

which is the strong form of (17). Thus,  $\psi/\Delta t$  from the Helmholtz decomposition is the new pressure from Chorin's projection scheme.  $\square$

In the case of mixed boundary conditions (1f), (1g) the space  $\Psi_D(\Omega)$  is replaced by

$$\Psi_M(\Omega) := \{q \in H^1(\Omega) \mid q = 0 \text{ a.e. on } \Gamma_N\} \quad (18)$$

employing homogeneous Dirichlet boundary conditions on  $\Gamma_N$ . This can be understood from (1g) which implies  $p \approx 0$  for small  $\mu$ , i.e. large Reynolds number. The irrotational part is defined as in (16) with  $\Psi_D(\Omega)$  replaced by  $\Psi_M(\Omega)$ , meaning that  $\psi$  satisfies homogeneous Neumann conditions on  $\Gamma_D$  and homogeneous Dirichlet conditions on  $\Gamma_N$ . Again,  $v \in H(\Omega)$  is uniquely defined (observe that now  $\Gamma_D \subset \partial\Omega$  in  $H(\Omega)$ ).

### 3.2. Discrete Helmholtz decomposition

We now seek discrete versions  $\mathcal{P}_h : \mathbf{X}_h^p \rightarrow \mathbf{X}_h^p$  of the Helmholtz projection operator  $\mathcal{P}$ . A direct reconstruction of the weakly divergence free velocity as  $v = w - \nabla\psi$  in DG splitting schemes is reported to be unstable when the spatial mesh is coarse and the time step is small [20, 21, 4] and several local postprocessing techniques are discussed in the literature. Here we propose a new postprocessing technique based on  $H(\text{div})$  reconstruction which is popular in porous media flows [22, 23]. These reconstructions are element-local, easy to compute and provide a locally mass conservative projected velocity, a property not shared by the reconstructions in [20, 4]. [21] takes into account inter-element continuity in a regularized least-squares sense but does not provide a projection. The construction presented here is easier to compute, provides exact local mass conservation, satisfies the discrete continuity equation exactly and provides a projection.

#### 3.2.1. Standard projection

For any given tentative velocity  $w_h \in \mathbf{X}_h^p$  the straightforward translation of the Helmholtz decomposition (17) in the DG setting reads

$$(v_h, \varphi)_{0,\Omega} + (\nabla\psi_h, \varphi)_{0,\Omega} = (w_h, \varphi)_{0,\Omega} \quad \forall \varphi \in \mathbf{X}_h^p, \quad (19a)$$

$$b(v_h, q) = r(q) \quad \forall q \in M_h^{p-1}. \quad (19b)$$

Note that the second equation requires the projected velocity to satisfy the discrete form of the continuity equation (8b). From the first condition (19a) we get  $v_h + \nabla\psi_h = w_h \Leftrightarrow v_h = w_h - \nabla\psi_h$  since all involved functions are in  $\mathbf{X}_h^p$ . Inserting this into (19a) yields an equation for  $\psi$ :

$$b(\nabla\psi_h, q) = b(w_h, q) - r(q) \quad \forall q \in M_h^{p-1}.$$

Using Observation 1 on the left hand side we get

$$b(\nabla\psi_h, q) = \sum_{E \in \mathcal{E}_h} (\nabla\psi_h, \nabla q)_{0,E} - \sum_{e \in \Gamma_h^{\text{int}}} (\{\nabla\psi_h\} \cdot n_e, [q])_{0,e} - \sum_{e \in \Gamma_h^N} (\nabla\psi_h \cdot n_e, q)_{0,e}. \quad (20)$$

This is part of the standard SIPG formulation of Poisson's equation with homogeneous Neumann boundary conditions on  $\Gamma^D$  with the stabilization terms missing. In order to stabilize, we define

$$j_0(\psi_h, q) = - \sum_{e \in \Gamma_h^{\text{int}}} (\{\nabla q\} \cdot n_e, [\psi_h])_{0,e} + \sum_{e \in \Gamma_h^{\text{int}}} \frac{\sigma}{h_e} ([q], [\psi_h])_{0,e} - \sum_{e \in \Gamma_h^N} (\nabla q \cdot n_e, \psi_h)_{0,e} + \sum_{e \in \Gamma_h^N} \frac{\sigma}{h_e} (q, \psi_h)_{0,e}. \quad (21)$$

and solve the *stabilized version*

$$\psi_h \in M_h^{p-1} : \quad \alpha(\psi_h, q) = b(w_h, q) - r(q) \quad \forall q \in M_h^{p-1} \quad (22)$$

where

$$\alpha(\psi_h, q) = b(\nabla\psi_h, q) + j_0(\psi_h, q).$$

Note that this system naturally corresponds to homogeneous Neumann conditions on  $\Gamma^D$  and homogeneous Dirichlet conditions on  $\Gamma^N$  (which might be empty). Now we may define the first projection scheme.

**Algorithm 1.** The standard projection  $\mathcal{P}_h^{\text{std}}$  is given by the following algorithm:

i) For any tentative velocity  $w_h \in \mathbf{X}_h^p$  solve

$$\psi_h \in M_h^{p-1} : \quad \alpha(\psi_h, q) = b(w_h, q) - r(q) \quad \forall q \in M_h^{p-1}. \quad (23)$$



ii) Set  $\mathcal{P}_h^{\text{std}} w_h = v_h$  where  $v_h$  solves

$$(v_h, \varphi)_{0,\Omega} = (w_h, \varphi)_{0,\Omega} - (\nabla \psi_h, \varphi)_{0,\Omega} \quad \forall \varphi \in \mathbf{X}_h^p. \quad (24)$$

This requires the solution of a mass matrix which is block-diagonal. Choosing an orthogonal basis it can even be diagonal and thus the computation is cheap. Note also that this implies  $v_h = w_h - \nabla \psi_h$  since  $\nabla \psi_h \in \mathbf{X}_h^p$ .

Unfortunately, this projection is reported to be unstable in the small time step limit [20] and we also observed this behaviour. Part of the problem is that  $\mathcal{P}_h^{\text{std}}$  is actually not a projection, i.e.  $(\mathcal{P}_h^{\text{std}})^2 \neq \mathcal{P}_h^{\text{std}}$ .

### 3.2.2. Div-div projection

In order to overcome the stability problem the authors in [4] suggested to stabilize the projection by an additional term in (24):

**Algorithm 2.** The div-div projection  $\mathcal{P}_h^{\text{div-div}}$  is given by the following algorithm:

i) For any tentative velocity  $w_h \in \mathbf{X}_h^p$  solve (same as before)

$$\psi_h \in M_h^{p-1} : \quad \alpha(\psi_h, q) = b(w, q) - r(q) \quad \forall q \in M_h^{p-1}.$$

ii) Set  $\mathcal{P}_h^{\text{div-div}} w_h = v_h$  where  $v_h$  solves

$$(v_h, \varphi)_{0,\Omega} + \tau_D (\nabla \cdot v_h, \nabla \cdot \varphi)_{0,\Omega} = (w_h, \varphi)_{0,\Omega} - (\nabla \psi_h, \varphi)_{0,\Omega} \quad \forall \varphi \in \mathbf{X}_h^p \quad (25)$$

where  $\tau_D$  is a user-supplied constant.

Again this requires the solution of an element-local system which is not diagonal. As reported in [4] and the examples below this gives good results with quite small point-wise divergence. However, the projected velocity does not satisfy a local mass conservation property and  $(\mathcal{P}_h^{\text{div-div}})^2 \neq \mathcal{P}_h^{\text{div-div}}$ .

### 3.2.3. Raviart-Thomas projection

The aim of this subsection is to reconstruct  $-\nabla \psi_h$  in the Raviart-Thomas space of degree  $k$  [35] on affine cuboid meshes given by

$$\mathbf{RT}_h^k = \{v \in H(\text{div}; \Omega) \mid v|_E \in \mathbf{RT}_E^k \forall E \in \mathcal{E}_h\} \quad (26)$$

with the Raviart-Thomas space on element  $E$  given by

$$\mathbf{RT}_E^k = \{v \in H(\text{div}; E) \mid v = T_E(\hat{v}), (\hat{v})_i = \sum_{\{\alpha \mid 0 \leq \alpha_j \leq k + \delta_{ij}\}} c_{i,\alpha} \hat{x}^\alpha\} \quad (27)$$

where we made use of the Piola transformation of the affine element  $E \in \mathcal{E}_h$ , i.e.  $\mu_E(\hat{x}) = B_E \hat{x} + b_E$ , defined as

$$T_E(\hat{v}) = \frac{1}{|\det B_E|} B_E \hat{v}.$$

For  $k > 0$  the construction needs also the space

$$\Psi_E^k = \{v \in H(\text{div}; E) \mid v = T_E(\hat{v}), (\hat{v})_i = \sum_{\{\alpha \mid 0 \leq \alpha_j \leq k - \delta_{ij}\}} c_{i,\alpha} \hat{x}^\alpha\}. \quad (28)$$

Note that in contrast to (27) the polynomial degree in direction  $i$  in component  $i$  is decreased instead of increased.

Assume that  $\psi_h \in M_h^{p-1}$  solves (22) as before. Following [23] we now compute  $\gamma_h = G_h \psi_h \in \mathbf{RT}_h^k$ ,  $k = p - 1$ , as reconstruction of  $-\nabla \psi_h$  as follows. On element  $E \in \mathcal{E}_h$  with faces  $e \in \partial E$  define

$$(\gamma_h \cdot n_e, q)_{0,e} = (-\{\nabla \psi\} \cdot n_e + \frac{\sigma}{h_e} [\psi_h], q)_{0,e} \quad e \in \Gamma_h^{\text{int}}, q \in Q_e^k, \quad (29a)$$

$$(\gamma_h \cdot n_e, q)_{0,e} = (-\nabla \psi \cdot n_e + \frac{\sigma}{h_e} \psi_h, q)_{0,e} \quad e \in \Gamma_h^N, q \in Q_e^k, \quad (29b)$$

$$(\gamma_h \cdot n_e, q)_{0,e} = 0 \quad e \in \Gamma_h^D, q \in Q_e^k, \quad (29c)$$

$$(29d)$$

and for  $k > 0$  define in addition

$$(\gamma_h, r)_{0,E} = -(\nabla \psi, r)_{0,E} + \frac{1}{2} \sum_{e \in \partial E \cap \Gamma_h^{\text{int}}} (r \cdot n_e, [\psi_h])_{0,e} + \sum_{e \in \partial E \cap \Gamma_h^N} (r \cdot n_e, \psi_h)_{0,e}, \quad \forall r \in \Psi_E^k. \quad (29e)$$

With this we can define our final projection method:

**Algorithm 3.** The RT projection  $\mathcal{P}_h^{\text{RT}}$  is given by the following algorithm:

i) For any tentative velocity  $w_h \in \mathbf{X}_h^p$  solve

$$\psi_h \in M_h^{p-1} : \quad \alpha(\psi_h, q) = b(w_h, q) - r(q) \quad \forall q \in M_h^{p-1}.$$

ii) Reconstruct  $\gamma_h = G_h \psi_h \in \mathbf{RT}_h^{p-1}$ .

iii) Set  $\mathcal{P}_h^{\text{RT}} w_h = v_h$  where  $v_h$  solves

$$(v_h, \varphi)_{0,\Omega} = (w_h, \varphi)_{0,\Omega} + (G_h \psi_h, \varphi)_{0,\Omega} \quad \forall \varphi \in \mathbf{X}_h^p.$$

This requires the solution of a (block-) diagonal system.

The reconstruction  $G_h$  defined above satisfies the following important property.

**Lemma 1.** Let  $\psi_h \in M_h^{p-1}$  solve  $\alpha(\psi_h, q) = l(q)$  for all  $q \in M_h^{p-1}$  and any linear right hand side functional  $l$ . Let furthermore  $\gamma_h = G_h \psi_h \in \mathbf{RT}_h^{p-1}$  be the reconstruction defined above. Then for every  $q \in Q_h^{p-1}$  and  $\chi_E$  the characteristic function of element  $E \in \mathcal{E}_h$  we have

$$(\nabla \cdot \gamma_h, q \chi_E)_{0,E} = l(q \chi_E). \quad (30)$$

*Proof.* Straightforward extension of Theorem 3.1 in [23] from simplicial to affine cuboid elements. Essential ingredients are that for any  $q \in Q_h^{p-1} \Rightarrow \nabla \psi|_E \in \Psi_E^k$  and the special definition of the right hand side in (29e).  $\square$

And with this lemma we can prove the following

**Theorem 2.** The projected velocity  $\mathcal{P}_h^{\text{RT}} w_h$  satisfies the discrete continuity equation exactly, i.e.

$$b(\mathcal{P}_h^{\text{RT}} w_h, q) = r(q) \quad \forall q \in M_h^{p-1}. \quad (31)$$

*Proof.* The characteristic functions form a partition of unity, i.e. for any  $q \in Q_h^{p-1}$  we have  $q = \sum_{E \in \mathcal{E}_h} q \chi_E$ . Inserting into the definition of  $b$ , observing that  $[\gamma_h] \cdot n_e = 0$  since  $\gamma_h \in H(\text{div}; \Omega)$  as well as  $\gamma_h \cdot n_e = 0$  due to (29c) and using Lemma 1 gives:

$$\begin{aligned} b(\mathcal{P}_h^{\text{RT}} w_h, q) &= b(w_h, q) + b(G_h \psi_h, q) \\ &= b(w_h, q) - \sum_{E \in \mathcal{E}_h} (\nabla \cdot \gamma_h, q \chi_E)_{0,E} + \sum_{e \in \Gamma_h^{\text{int}}} ([\gamma_h] \cdot n_e, \{q\})_{0,e} + \sum_{e \in \Gamma_h^D} (\gamma_h \cdot n_e, q)_{0,e} \\ &= b(w_h, q) - \sum_{E \in \mathcal{E}_h} l(q \chi_E) = b(w_h, q) - \sum_{E \in \mathcal{E}_h} [b(w_h, q \chi_E) - r(q \chi_E)] \\ &= b(w_h, q) - b(w_h, q) + r(q) = r(q) \end{aligned} \quad (32)$$

$\square$

**Remark 2.** As corollaries we have

- 1) The projected velocity  $v_h = \mathcal{P}_h^{\text{RT}} w_h$  satisfies a discrete conservation property (just insert a characteristic function  $\chi_E$  as test function). Note that a discrete conservation property can be achieved with reconstruction in Raviart-Thomas space with degree  $k \leq p-1$ .
- 2)  $(\mathcal{P}_h^{\text{RT}})^2 = \mathcal{P}_h^{\text{RT}}$  follows from the fact that  $l(q) = b(\mathcal{P}_h^{\text{RT}} w_h, q) - r(q) = 0$  is the right hand side of (22).

The discrete continuity equation does not imply that the divergence of the projected velocity vanishes point-wise. The following Lemma shows that the divergence in the interior of elements is controlled in an integral sense only by the jumps of the tentative velocity:

**Lemma 2.** The projected velocity  $v_h = \mathcal{P}_h^{\text{RT}} w_h$  satisfies for all  $q \in M_h^{p-1}$ ,  $E \in \mathcal{E}_h$  and  $q_E = q\chi_E$ :

$$(\nabla \cdot v_h, q_E)_{0,E} = \frac{1}{2} \sum_{e \in \Gamma_h^{\text{int}} \cap \partial E} ([w_h] \cdot n_e, q_E)_{0,e} + \sum_{e \in \Gamma_h^D \cap \partial E} ((w_h - g) \cdot n_e, q_E)_{0,e}. \quad (33)$$

*Proof.* Using Lemma 1 we get

$$\begin{aligned} (\nabla \cdot v_h, q_E)_{0,E} &= (\nabla \cdot w_h, q_E)_{0,E} + (\nabla \cdot \gamma_h, q_E)_{0,E} = (\nabla \cdot w_h, q_E)_{0,E} + l(q_E) \\ &= (\nabla \cdot w_h, q_E)_{0,E} + b_h(w_h, q_E) - r(q_E) \\ &= (\nabla \cdot w_h, q_E)_{0,E} - (\nabla \cdot w_h, q_E)_{0,E} + \frac{1}{2} \sum_{e \in \Gamma_h^{\text{int}} \cap \partial E} ([w_h] \cdot n_e, q_E)_{0,e} + \sum_{e \in \Gamma_h^D \cap \partial E} ((w_h - g) \cdot n_e, q_E)_{0,e}. \end{aligned} \quad (34)$$

□

### 3.3. Pressure-correction schemes

Since the nonlinear term in the Navier-Stokes equations does not play an essential role in the derivation of the projection methods we hereafter consider the instationary Stokes equations. The equations in the subproblems arise from the method of lines discretization.

#### 3.3.1. Incremental pressure-correction scheme (IPCS)

The IPCS is a straightforward way to split between incompressibility and dynamics. In the viscous substep the pressure is made explicit that we denote by  $p_h^{\star, k+1}$ . In the second substep a pressure correction is computed to accordingly correct the velocity. The particular choice of the time discretization is not important. It is possible to use the implicit Euler time stepping or second order time stepping methods such as BDF2 or Alexander's second order strongly S-stable scheme [36]. The semi-discretized in space splitting scheme then reads as follows:

1. Tentative velocity step, compute  $\tilde{v}_h^{k+1}$ :

$$\rho(\partial_t v_h, \varphi_h) + \mu a(v_h, \varphi_h) + b(\varphi_h, p_h^{\star, k+1}) = l(\varphi_h) \quad \forall \varphi_h \in \mathbf{X}_h^p$$

2. Pressure Poisson equation, compute correction  $\delta p_h^{k+1}$ :

$$\alpha(\delta p_h^{k+1}, q_h) = \frac{1}{\Delta t^{k+1}} (b(\tilde{v}_h^{k+1}, q_h) - r(q_h)) \quad \forall q_h \in M_h^{p-1}$$

3. Post-processing  $v_h^{k+1} = \mathcal{P}_h \tilde{v}_h^{k+1}$  with  $\psi_h = \Delta t^{k+1} \delta p_h^{k+1}$ , using one of the variants  $\mathcal{P}_h^{\text{std}}$ ,  $\mathcal{P}_h^{\text{div-div}}$ ,  $\mathcal{P}_h^{\text{RT}}$ .

4. Pressure update:

$$p_h^{k+1} = p_h^{\star, k+1} + \delta p_h^{k+1}.$$

The choice  $p_h^{\star, k+1} = 0$ , implicit Euler as time stepping yields to Chorin's projection method. Constant extrapolation  $p_h^{\star, k+1} = p_h^k$  gives the IPCS. The IPCS introduces the artificial boundary conditions for the pressure correction which lead to the series of equalities

$$\partial_n p_h^{k+1}|_{\Gamma_D} = \dots = \partial_n p_h^1|_{\Gamma_D} = \partial_n p_h^0|_{\Gamma_D} \quad (35)$$

$$p_h^{k+1}|_{\Gamma_N} = \dots = p_h^1|_{\Gamma_N} = p_h^0|_{\Gamma_N} \quad (36)$$

for the pressure itself over time. In the purely Dirichlet case, i.e.  $\Gamma_N = \emptyset$ , the scheme is fully first-order accurate even if the implicit Euler time stepping is used. But when  $\Gamma_N \neq \emptyset$  the order of approximation of the velocity in the  $H_0^1$ -norm and of the pressure in the  $L^2$ -norm is degraded due to the homogeneous Dirichlet boundary conditions for the pressure.

There is little improvement regarding the order of the scheme when a second order time stepping method is used. In the purely Dirichlet case the scheme is fully second order on the velocity in the  $L^2$ -norm but it stays first order on the velocity in the  $H_0^1$ -norm and on the pressure in the  $L^2$ -norm. For  $\Gamma_N \neq \emptyset$  the approximation order even stays the same.

The constant extrapolation for the explicit pressure in the momentum equation implies that the scheme has an irreducible splitting error of  $\mathcal{O}(\Delta t^2)$ . Hence using a higher than second order time discretization does not improve the overall accuracy.

### 3.3.2. Rotational incremental pressure-correction scheme (RIPCS)

One reason for the above scheme to have poor convergence properties especially when outflow boundary conditions are present is that the pressure boundary conditions stay constant over time. To overcome this difficulty it was first introduced by Timmermans, Mineev and Van De Vosse [14] to use the *rotational form* of the Laplacian, namely

$$-\Delta v = \nabla \times (\nabla \times v) - \nabla(\nabla \cdot v). \quad (37)$$

To understand why this modification performs better we consider for simplicity the momentum equation in classical form and insert the rotational form of the Laplacian:

$$\frac{\tilde{v}_h^{k+1} - v_h^k}{\Delta t^{k+1}} + \mu \nabla \times (\nabla \times \tilde{v}_h^{k+1}) + \nabla(p_h^{\star, k+1} - \mu \nabla \cdot \tilde{v}_h^{k+1}) = f(t^{k+1}) \quad (38)$$

where  $p_h^{\star, k+1}$  is as before an approximation of  $p(t^{k+1})$ . Eliminating the tentative velocity  $\tilde{v}_h^{k+1} = v_h^{k+1} + \Delta t^{k+1} \nabla \delta p_h^{k+1}$  with the Helmholtz decomposition gives

$$\frac{v_h^{k+1} - v_h^k}{\Delta t^{k+1}} + \mu \nabla \times (\nabla \times \tilde{v}_h^{k+1}) + \nabla(\delta p_h^{k+1} + p_h^{\star, k+1} - \mu \nabla \cdot \tilde{v}_h^{k+1}) = f(t^{k+1}). \quad (39)$$

Thus the quantity  $\delta p_h^{k+1} + p_h^{\star, k+1} - \mu \nabla \cdot \tilde{v}_h^{k+1}$  can be interpreted as an approximation of the pressure. Hence retaining the time step with the momentum equation the tables can be turned to obtain the *incremental pressure-correction scheme in rotational form*:

1. Tentative velocity step, compute  $\tilde{v}_h^{k+1}$ :

$$\rho(\partial_t v_h, \varphi_h) + \mu a(v_h, \varphi_h) + b(\varphi_h, p_h^{\star, k+1}) = l(\varphi_h) \quad \forall \varphi_h \in \mathbf{X}_h^p$$

2. Pressure Poisson equation, compute correction  $\delta p_h^{k+1}$ :

$$\alpha(\delta p_h^{k+1}, q_h) = \frac{1}{\Delta t^{k+1}} (b(\tilde{v}_h^{k+1}, q_h) - r(q_h)) \quad \forall q_h \in M_h^{p-1}$$

3. Post-processing  $v_h^{k+1} = \mathcal{P}_h \tilde{v}_h^{k+1}$  with  $\psi_h = \Delta t^{k+1} \delta p_h^{k+1}$ , using one of the variants  $\mathcal{P}_h^{\text{std}}, \mathcal{P}_h^{\text{div-div}}, \mathcal{P}_h^{\text{RT}}$ .

4. Pressure update with scaling factor  $\omega$ :

$$(p_h^{k+1}, q_h) = (\omega \delta p_h^{k+1} + p_h^{\star, k+1}, q_h) + \mu(b(\tilde{v}_h^{k+1}, q_h) - r(q_h)) \quad \forall q_h \in M_h^{p-1}.$$

The scaling factor is usually set to  $\omega = 1$  for first order time stepping schemes and to  $\omega = \frac{3}{2}$  for second order time stepping schemes.

The contribution  $\nabla \cdot \tilde{v}_h^{k+1}$  improves the accuracy of the scheme such that it is first order accurate for both Dirichlet and outflow boundary conditions. The use of a second order time stepping scheme improves the convergence rate on the velocity in the  $H_0^1$ -norm and on the pressure in the  $L^2$ -norm to  $\frac{3}{2}$  when  $\Gamma_N = \emptyset$ . In the presence of outflow boundary conditions the convergence rate  $\frac{3}{2}$  for the velocity in the  $L^2$ -norm is likely to be the best possible whereas the convergence rate in the  $H_0^1$ -norm for the velocity and in the  $L^2$ -norm for the pressure is limited to 1. As in the IPCS higher than second order time stepping schemes do not improve the overall accuracy.

## 4. Numerical experiments

We start the numerical experiments by cross-comparing the pointwise divergence and local mass conservation for the div-div stabilization and the  $H(\text{div})$  reconstruction. Then we illustrate the convergence properties of the IPCS and RIPCIS for global Dirichlet boundary conditions 4.3, mixed boundary conditions 4.4, periodic boundary conditions 4.5 and also in 3D using the Beltrami flow problem 4.6. Both schemes are tested in their second order formulation. Temporal convergence is analyzed for the Taylor-Hood-like DG-spaces  $\mathcal{Q}_2/\mathcal{Q}_1$ ,  $\mathcal{Q}_3/\mathcal{Q}_2$ ,  $\mathcal{Q}_4/\mathcal{Q}_3$  and also local mass conservation - given as the right-hand side of (11) - is investigated.

### 4.1. Solvers and Implementation

The parallel solver has been implemented in a high-performance C++ code based on the DUNE discretization framework [37, 38]. The assembly of residuals and jacobians uses spectral discontinuous Galerkin methods. Sum-factorization technique for tensor product bases is employed that reduce the computational complexity significantly. Every velocity component underlies the same ansatz space. Therefore sum-factorization applied to the scalar convection-diffusion equation as described in [5] can be expanded in a straightforward way to the subproblems in the splitting schemes. The viscous substep is solved with a matrix-free Newton method with a single block SOR preconditioner in GMRes as a linear solver. The pressure Poisson equation is solved with hybrid AMG-DG preconditioner where the correction in the conforming  $\mathcal{Q}_1$  subspace is rediscritized, [39, 28] and the matrix on the DG level is not required for this purpose. Thus it is possible to do either matrix-free or matrix-based operator application and smoothing on the DG level.

### 4.2. Local mass conservation

We consider the Navier-Stokes equations on the domain  $\Omega = (-1, 1)^2$  and take the two dimensional Taylor-Green vortex which has been studied before by [40, 8, 41]. In two dimensions the Taylor-Green vortex possesses the exact solution

$$\begin{aligned} v_1(x, y, t) &= -e^{-2\pi^2 \nu t} \cos(\pi x) \sin(\pi y) \\ v_2(x, y, t) &= e^{-2\pi^2 \nu t} \sin(\pi x) \cos(\pi y) \\ p(x, y, t) &= -0.25 \rho e^{-4\pi^2 \nu t} (\cos(2\pi y) + \cos(2\pi x)) . \end{aligned} \tag{40}$$

The source term is given by  $f = 0$ . We set  $\rho = 1$ ,  $\mu = 1/100$  and  $\nu = \mu/\rho$ . Periodic boundary conditions are imposed in both the  $x$  and  $y$  directions. We do the computations on a  $160 \times 160$  cubic mesh. The discussion on the temporal convergence rates is postponed to 4.5.

We start the discussion on the choice of order in the Raviart-Thomas space. We have shown in Theorem 2 that for  $\mathbf{RT}_{p-1}$  it holds: (I)  $(\mathcal{P}_h^{\text{RT}})^2 = \mathcal{P}_h^{\text{RT}}$ , (II) the reconstructed velocity satisfies the continuity equation and (III) is locally mass conservative. However a naive approach by looking at the dimension of the local function space of  $\nabla_h M_h^{p-1}$  also accounts to possibly choose  $\mathbf{RT}_{p-2}$ . As stated in Remark 2 local mass conservation can still be achieved with reconstruction in Raviart-Thomas space of degree  $p-2$ . This is demonstrated on the right of figure 2 and notably we get the same distribution with  $\mathbf{RT}_{p-1}$ . Moreover numerical experiments with the power iteration applied to the operator  $\mathcal{P}_h^{\text{RT}}$  have shown that  $(\mathcal{P}_h^{\text{RT}})^2 \tilde{v}_h^{k+1} = \mathcal{P}_h^{\text{RT}} \tilde{v}_h^{k+1}$  also for  $\mathbf{RT}_{p-2}$ . Table 2 - 3 compare the temporal accuracy between the discretization triples  $\mathcal{Q}_2/\mathcal{Q}_1/\text{RT}_0$ ,  $\mathcal{Q}_2/\mathcal{Q}_1/\text{RT}_1$ . It can be seen that there is no significant difference on the error at final time. Reconstruction in the  $\mathbf{RT}_{p-2}$  space provides thus to be a sufficient alternative in the splitting algorithm.

Next we want to cross-compare the temporal accuracy for the spatial discretizations  $\mathcal{Q}_2/\mathcal{Q}_1$ ,  $\mathcal{Q}_3/\mathcal{Q}_2$  with div-div stabilization and  $\mathcal{Q}_2/\mathcal{Q}_1/\text{RT}_0$ ,  $\mathcal{Q}_3/\mathcal{Q}_2/\text{RT}_1$ . Table 1 - 2 show the errors for the RIPCS  $\mathcal{Q}_2/\mathcal{Q}_1$  with div-div stabilization and the RIPCS  $\mathcal{Q}_2/\mathcal{Q}_1/\text{RT}_0$  and table 4 - 5 the errors for the RIPCS  $\mathcal{Q}_3/\mathcal{Q}_2$  with div-div stabilization and the RIPCS  $\mathcal{Q}_3/\mathcal{Q}_2/\text{RT}_1$ , respectively. There is no significant difference in the temporal behaviour for both pairs, a logarithmic plot of the errors would lead to indistinguishable curves. Thus for the upcoming investigation on the convergence properties we will use the div-div stabilization technique because it is an inexpensive alternative to the  $H(\text{div})$  reconstruction which is at the time only implemented up to order one. Note that the errors in the tables 1, 4 are also contained in the figures of 5.

dt	$L^2$ error $v$	$H_0^1$ error $v$	$L^2$ error $p$
2.000e-01	3.89336e-02	3.12769e-01	2.24301e-02
1.000e-01	1.00536e-02	7.86088e-02	6.49292e-03
5.000e-02	2.54833e-03	1.96963e-02	2.07180e-03
2.500e-02	6.40802e-04	5.00184e-03	7.85322e-04
1.250e-02	1.60275e-04	1.93785e-03	3.74214e-04
6.250e-03	3.99586e-05	1.67405e-03	2.24884e-04

Table 1: Errors for the Taylor-Green vortex at final time T=2 obtained by RIPCS and  $\mathcal{Q}_2/\mathcal{Q}_1$  with div-div stabilization

dt	$L^2$ error $v$	$H_0^1$ error $v$	$L^2$ error $p$
2.000e-01	3.89026e-02	3.06282e-01	2.24215e-02
1.000e-01	1.00444e-02	7.72283e-02	6.49243e-03
5.000e-02	2.54548e-03	1.96643e-02	2.07260e-03
2.500e-02	6.39597e-04	5.44801e-03	7.86167e-04
1.250e-02	1.59573e-04	2.63178e-03	3.75384e-04
6.250e-03	3.97373e-05	2.33037e-03	2.27288e-04

Table 2: Errors for the Taylor-Green vortex at final time T=2 obtained by RIPCS and  $\mathcal{Q}_2/\mathcal{Q}_1/\text{RT}_0$

dt	$L^2$ error $v$	$H_0^1$ error $v$	$L^2$ error $p$
2.000e-01	3.88824e-02	3.03453e-01	2.24163e-02
1.000e-01	1.00387e-02	7.71449e-02	6.49254e-03
5.000e-02	2.54417e-03	1.96504e-02	2.07356e-03
2.500e-02	6.39432e-04	5.44560e-03	7.86989e-04
1.250e-02	1.59699e-04	2.63182e-03	3.75972e-04
6.250e-03	3.99134e-05	2.33056e-03	2.27698e-04

Table 3: Errors for the Taylor-Green vortex at final time T=2 obtained by RIPCS and  $\mathcal{Q}_2/\mathcal{Q}_1/\text{RT}_1$

dt	$L^2$ error $v$	$H_0^1$ error $v$	$L^2$ error $p$
2.000e-01	3.88929e-02	3.03675e-01	2.23165e-02
1.000e-01	1.00411e-02	7.70569e-02	6.38400e-03
5.000e-02	2.54558e-03	1.94734e-02	1.96199e-03
2.500e-02	6.40610e-04	4.89254e-03	6.72911e-04
1.250e-02	1.60670e-04	1.22611e-03	2.60387e-04
6.250e-03	4.02320e-05	3.06909e-04	1.11552e-04

Table 4: Errors for the Taylor-Green vortex at final time  $T=2$  obtained by RIPCS and  $\mathcal{Q}_3/\mathcal{Q}_2$  with div-div stabilization

dt	$L^2$ error $v$	$H_0^1$ error $v$	$L^2$ error $p$
2.000e-01	3.88969e-02	3.03581e-01	2.23175e-02
1.000e-01	1.00423e-02	7.70650e-02	6.38402e-03
5.000e-02	2.54588e-03	1.94755e-02	1.96185e-03
2.500e-02	6.40684e-04	4.89306e-03	6.72797e-04
1.250e-02	1.60689e-04	1.22624e-03	2.60320e-04
6.250e-03	4.02364e-05	3.06934e-04	1.11516e-04

Table 5: Errors for the Taylor-Green vortex at final time  $T=2$  obtained by RIPCS and  $\mathcal{Q}_3/\mathcal{Q}_2/\text{RT}_1$

In figure 1 the pointwise divergence for  $p = 2$  on each mesh element is presented. The element-local div-div stabilization leads to smaller pointwise divergence than obtained with the  $H(\text{div})$  reconstruction. But it does not really cure the error on the local mass conservation. Compared to the standard  $L^2$ -projection the div-div stabilization reduces the values of the pointwise divergence and local mass conservation. The magnitude of the pointwise divergence from the  $H(\text{div})$  reconstruction is in between the magnitudes from stabilized and unstabilized variant, it is not identically zero as predicted by Lemma 2. The distribution of the divergence error with  $\mathcal{Q}_2/\mathcal{Q}_1/\text{RT}_1$  is similar and has the same maximum.

Figure 2 shows the error on local mass conservation for  $p = 2$ . According to our discussion at the beginning of 4.2 this appealing conservation property is perfectly fulfilled for the  $\mathbf{RT}_{p-1}$  and  $\mathbf{RT}_{p-2}$  reconstructions of the Helmholtz correction.

#### 4.3. Global Dirichlet boundary conditions

We consider the Stokes equations on the domain  $\Omega = (0, 1)^2$  and take the exact solution to be

$$\begin{aligned}
v_1(x, y, t) &= \sin(x + t) \sin(y + t) \\
v_2(x, y, t) &= \cos(x + t) \cos(y + t) \\
p(x, y, t) &= \sin(x - y + t) .
\end{aligned} \tag{41}$$

The source term is given by  $f = \partial_t v - \Delta v + \nabla p$ . The density and viscosity are both set to  $\rho = \mu = 1$ . Computations were done on a  $160 \times 160$  cubic mesh.

Figure 3 shows the error and the convergence rates as function of  $\Delta t$  for the IPCS and RIPCS. The green curves show the  $L^2$ -error for the velocity, the red curves the  $H_0^1$ -error for the velocity and the blue curves the  $L^2$ -error for the pressure obtained by the polynomial degrees  $p = 2, 3, 4$ . The curves grouped by the same color are almost identical meaning that the splitting error is dominant in the measured range of  $\Delta t$ . Therefore we have left out the curves with  $p = 4$  on the right for the sake of clarity. A transition towards smaller time steps causes earlier flattening out of the error curves the lower the spatial order is. This emerges at first for the  $H_0^1$ -error for the velocity and  $L^2$ -error for the pressure. This is demonstrated for the Taylor-Green vortex solution in section 4.5, c.f. right of figure 5.

Theory states that the solution of the second order IPCS satisfies the following error estimates: (I)  $L^2$ -velocity:  $\mathcal{O}(\Delta t^2)$  (II)  $H_0^1$ -velocity,  $L^2$ -pressure:  $\mathcal{O}(\Delta t)$ . On the left of figure 3 it is observed that the velocity

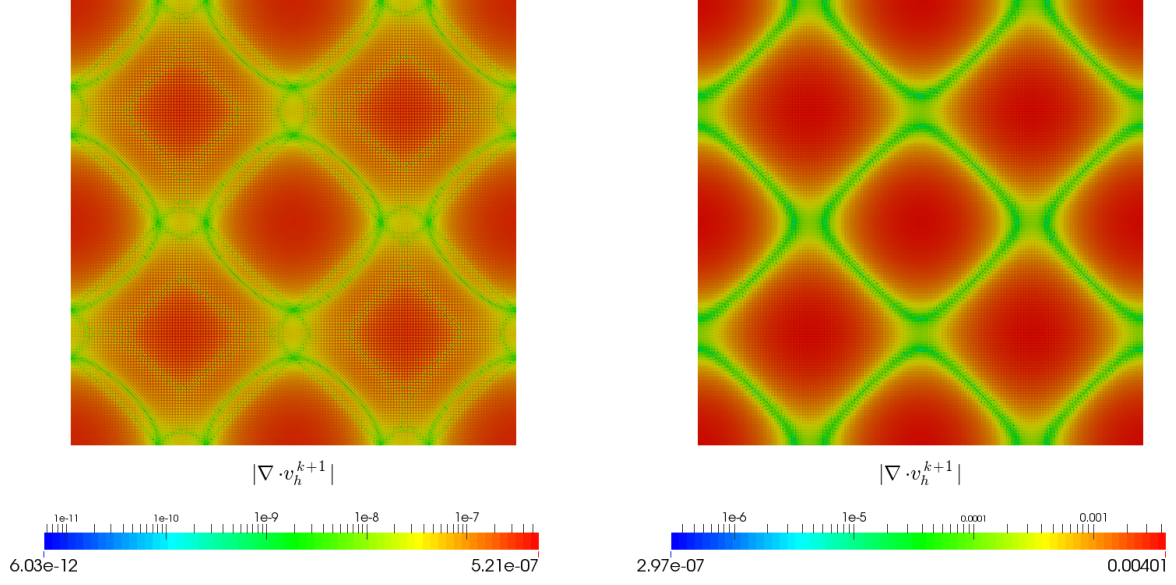


Figure 1: Pointwise divergence of the Taylor-Green vortex solution at time 1 with  $\Delta t = 0.025$  obtained by the RIPCS. Left part shows  $Q_2/Q_1$  with div-div stabilization. Right part shows  $Q_2/Q_1/RT_0$ .

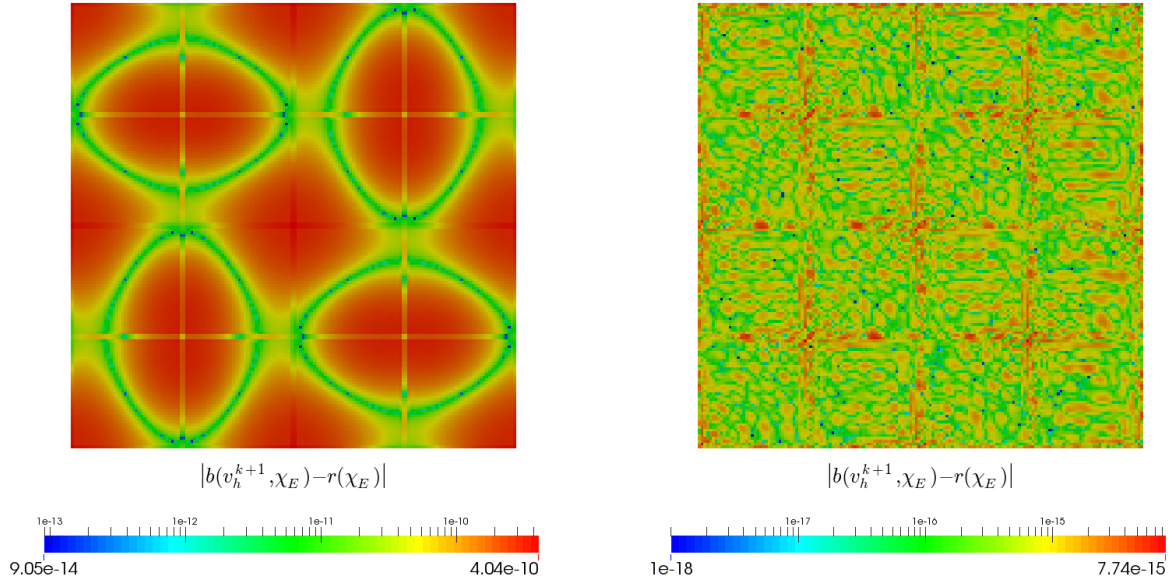


Figure 2: Local mass conservation of the Taylor-Green vortex solution at time 1 with  $\Delta t = 0.025$  obtained by the RIPCS. Left part shows  $Q_2/Q_1$  with div-div stabilization. Right part shows  $Q_2/Q_1/RT_0$ , identical to  $Q_2/Q_1/RT_1$ .



error in the  $L^2$ -norm is second order accurate, in the other two error measures the rate is 1.5 which is better than the prediction. Now the solution of the RIPCPS satisfies the following error estimates: (I)  $L^2$ -velocity:  $\mathcal{O}(\Delta t^2)$  (II)  $H_0^1$ -velocity,  $L^2$ -pressure:  $\mathcal{O}(\Delta t^{\frac{3}{2}})$ . The convergence rates on the right of figure 3 are consistent with the error estimates. Note that the  $L^2$ -errors on the velocity and pressure are almost identical in the results presented in [16]. The reason for the slight difference is likely to be the usage of BDF2 in [16] as time stepping.

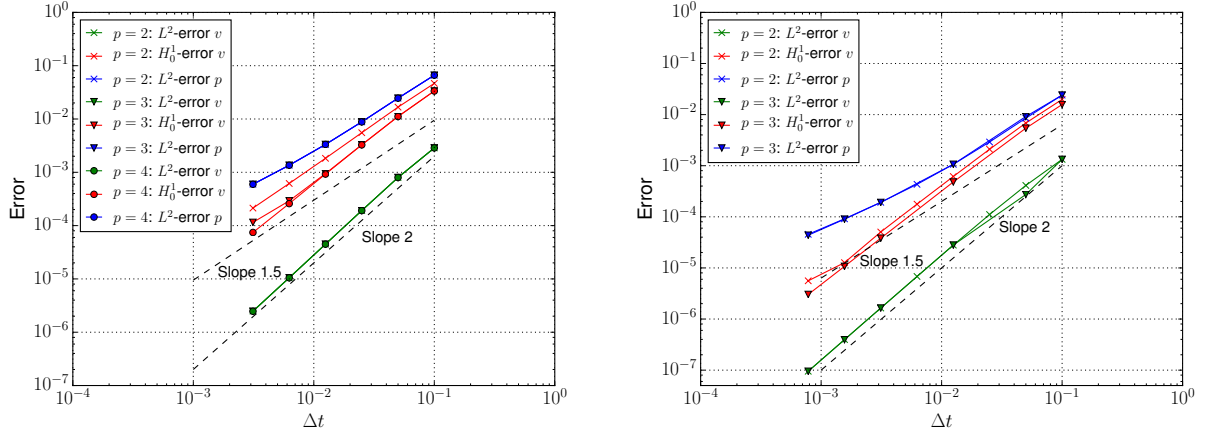


Figure 3: Errors and convergence rates at final time  $T=1$  for the global Dirichlet problem and spatial discretizations  $\mathcal{Q}_2/\mathcal{Q}_1$ ,  $\mathcal{Q}_3/\mathcal{Q}_2$ ,  $\mathcal{Q}_4/\mathcal{Q}_3$ . Left part shows the IPCS. Right part shows the RIPCPS.

A consideration of local mass conservation shows that it is well satisfied in the interior of the domain for the div-div stabilization. However the largest values  $\sim 10^{-9}$  are located in the cells that share an edge with the boundary. This is due to the artificial boundary conditions on the pressure.

The situation is different for the  $H(\text{div})$  reconstruction. In that case the distribution is similar to the right in figure 2 with  $\max_E |b(v_h^{k+1}, \chi_E) - r(\chi_E)| \sim 5 \cdot 10^{-14}$ .

#### 4.4. Mixed boundary conditions

We consider again the Stokes equations on the domain  $\Omega = (0, 1)^2$  and take the exact solution to be

$$\begin{aligned} v_1(x, y, t) &= \sin x \sin(y + t) \\ v_2(x, y, t) &= \cos x \cos(y + t) \\ p(x, y, t) &= \cos x \sin(y + t) . \end{aligned} \quad (42)$$

The source term is again given by  $f = \partial_t v - \Delta v + \nabla p$ . The density and viscosity are both set to  $\rho = \mu = 1$ . The outflow boundary is located at  $\Gamma_N = \{(x, y) \in \partial\Omega \mid x = 0\}$ . Computations were done on  $160 \times 160$  cubic mesh.

Figure 4 shows the error and the convergence rates as function of  $\Delta t$  for the IPCS and RIPCPS. The green curves show the  $L^2$ -error for the velocity, the red curves the  $H_0^1$ -error for the velocity and the blue curves the  $L^2$ -error for the pressure obtained by the polynomial degrees  $p = 2, 3, 4$ . The curves grouped by the same color are almost identical meaning that the splitting error is dominant in the measured range of  $\Delta t$ . Therefore we have left out the curves with  $p = 3$  on the left and  $p = 4$  on the right for the sake of clarity. A transition towards smaller time steps causes earlier flattening out of the error curves the lower the spatial order is. This emerges at first for the  $H_0^1$ -error for the velocity and  $L^2$ -error for the pressure. This is demonstrated for the Taylor-Green vortex solution in section 4.5, c.f. right of figure 5.

The solution of the IPCS satisfies the following error estimates: (I)  $L^2$ -velocity:  $\mathcal{O}(\Delta t)$  (II)  $H_0^1$ -velocity,  $L^2$ -pressure:  $\mathcal{O}(\Delta t^{\frac{1}{2}})$  which are identical to the first order IPCS. The results on the left of figure 4 indeed

show that the pressure approximation is poor due to the homogeneous Dirichlet boundary condition imposed on  $\Gamma_N$ . The RIPCS delivers improved error estimates in presence of mixed boundary conditions: (I)  $L^2$ -velocity:  $\mathcal{O}(\Delta t^{\frac{3}{2}})$  (II)  $H_0^1$ -velocity,  $L^2$ -pressure:  $\mathcal{O}(\Delta t)$ . The convergence rates on right of figure 4 are consistent with those estimates. Furthermore the error on the velocity in the  $L^2$ -norm behaves like  $\mathcal{O}(\Delta t^{\frac{5}{3}})$  which is also observed in Guermond, Mineev and Shen [18, 24]. The error in the  $H_0^1$ -norm is close to  $\mathcal{O}(\Delta t^{\frac{5}{4}})$  which is higher than the rate  $\mathcal{O}(\Delta t)$  predicted by theory. Note that [18, 24] have used BDF2 as time stepping for this problem and therefore the error curves are almost identical.

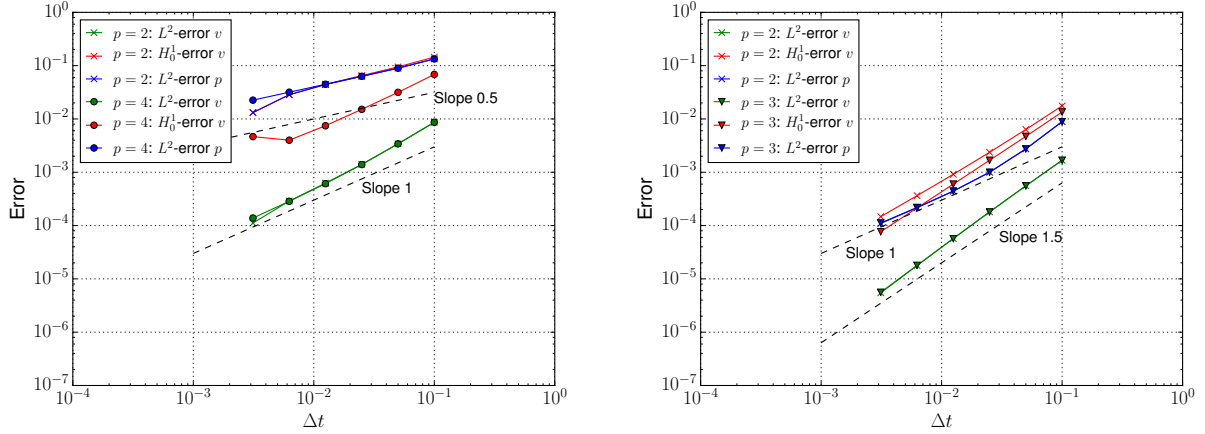


Figure 4: Errors and convergence rates at final time  $T=1$  for the mixed boundary condition problem and spatial discretizations  $\mathcal{Q}_2/\mathcal{Q}_1$ ,  $\mathcal{Q}_3/\mathcal{Q}_2$ ,  $\mathcal{Q}_4/\mathcal{Q}_3$ . Left part shows the IPCS. Right part shows the RIPCS.

Another consideration of local mass conservation shows that it is well satisfied in the interior of the domain. But due to the homogeneous Dirichlet boundary conditions for the pressure imposed on  $\Gamma_N$ , the largest errors  $\sim 10^{-7}$  are located in the cells next to outflow boundary.

With the  $H(\text{div})$  reconstruction we have  $\max_E |b(v_h^{k+1}, \chi_E) - r(\chi_E)| \sim 5 \cdot 10^{-14}$  whereat the maximum also occurs in the boundary cells.

#### 4.5. Periodic boundary conditions

We continue with the configuration and test problem presented in 4.2. Figure 5 shows the error and convergence rates as a function of  $\Delta t$  for the IPCS and RIPCS. The green curves show the  $L^2$ -error for the velocity, the red curves the  $H_0^1$ -error for the velocity and the blue curves the  $L^2$ -error for the pressure obtained by the polynomial degrees  $p = 2, 3$ . The results for  $p = 4$  are almost identical to  $p = 3$ , therefore it has been omitted for the sake of clarity. For the IPCS the curves grouped by the same color are almost identical meaning that the splitting error is dominant in the measured range of  $\Delta t$ . Note however that for  $p = 2$  in the RIPCS the spatial error is already not negligible in this range and becomes all-dominant for additionally smaller time steps taken. It can be seen on the right that the  $H_0^1$ -error on the velocity and  $L^2$ -error on the pressure flattens out whereas the errors from spatial order three continue decreasing with the same rate. That puts in favour higher polynomial degrees since the error on the same spatial mesh for moderate time step sizes is minimized.

There is no rigorous error analysis of the projection methods for purely periodic boundary conditions. But since in the periodic case no artificial boundary conditions are imposed on the pressure, both the standard and rotational formulation are expected to be fully second order accurate. This is validated for the pressure-correction schemes in figure 5. The error of the RIPCS is slightly lower than the error of the IPCS, but both schemes have the same convergence rate. It is close to  $\mathcal{O}(\Delta t^2)$  in the  $L^2$ -norm on the pressure while the rates of the velocity in the  $L^2$ -norm and  $H_0^1$ -norm are perfectly of second order.

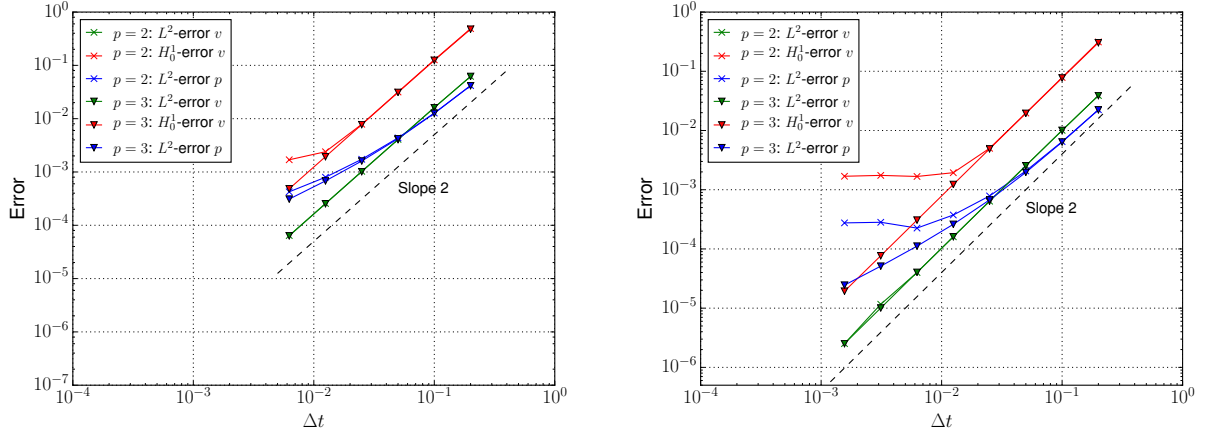


Figure 5: Errors and convergence rates at final time  $T=2$  for the periodic boundary condition problem and spatial discretizations  $\mathcal{Q}_2/\mathcal{Q}_1$ ,  $\mathcal{Q}_3/\mathcal{Q}_2$ ,  $\mathcal{Q}_4/\mathcal{Q}_3$ . Left part shows the IPCS. Right part shows the RIPCS.

The absence of artificial boundary conditions also implies that the error on local mass conservation is distributed over the interior on the domain. This was shown before in figure 2.

#### 4.6. Beltrami flow

The Beltrami flow is one of the rare test problems where an exact fully three-dimensional solution of the Navier-Stokes equations is derived. It has its origin from [42] and has been later studied by [43]. The domain is  $\Omega = (-1, 1)^3$  and global Dirichlet boundary conditions are imposed by the exact solution

$$\begin{aligned}
 v_1(x, y, z, t) &= -a e^{-d^2 t} (e^{ax} \sin(dz + ay) + \cos(dy + ax) e^{az}) \\
 v_2(x, y, z, t) &= -a e^{-d^2 t} (e^{ax} \cos(dz + ay) + e^{ay} \sin(az + dx)) \\
 v_3(x, y, z, t) &= -a e^{-d^2 t} (e^{ay} \cos(az + dx) + \sin(dy + ax) e^{az}) \\
 p(x, y, z, t) &= -0.5 a^2 \rho e^{-d^2 t} (2 \cos(dy + ax) e^{a(z+x)} \sin(dz + ay) \\
 &\quad + 2 e^{a(y+x)} \sin(az + dx) \cos(dz + ay) \\
 &\quad + 2 \sin(dy + ax) e^{a(z+y)} \cos(az + dx) + e^{2az} + e^{2ay} + e^{2ax}).
 \end{aligned} \tag{43}$$

The Beltrami flow has the property that the velocity and vorticity vectors are aligned, namely  $d v - \nabla \times v = 0$ . The source term is given by  $f = 0$ , the density, viscosity are set to  $\rho = \mu = 1$ . The constants  $a$  and  $d$  may be chosen arbitrarily and have been set to  $a = \pi/4$ ,  $d = \pi/2$  as in [42]. Computations were done on a  $50 \times 50 \times 50$  cubic mesh.

Figure 6 shows the error and convergence rates as a function of  $\Delta t$  for the RIPCS. The green curves show the  $L^2$ -error for the velocity and the red curves the  $H_0^1$ -error for the velocity obtained by the polynomial degrees  $p = 2, 3$ . The curves grouped by the same color are almost identical meaning that the splitting error is dominant in the measured range of  $\Delta t$ . It can be concluded from the figure that error is fully second order convergent in both norms.

#### 4.7. 3D DNS of turbulent flows

We test the applicability of the code to direct numerical simulations (DNS) with two examples.

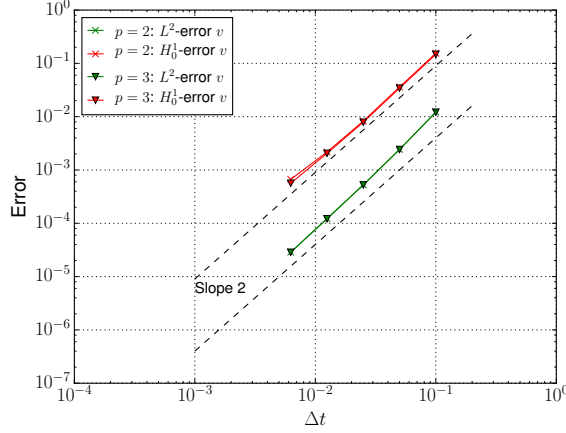


Figure 6: Errors and convergence rates at final time  $T=0.5$  for the Beltrami test problem using the RIPCS with the spatial discretizations  $\mathcal{Q}_2/\mathcal{Q}_1$ ,  $\mathcal{Q}_3/\mathcal{Q}_2$ .

#### 4.7.1. 3D Driven Cavity

The driven cavity flow is a commonly used benchmark problem due to its simple geometry. We take the configuration based on [44]. We shift the domain to  $\Omega = (0, 1)^3$  instead, set  $\rho = 1$  and  $\text{Re} = 1/\mu = 10000$ . The driving velocity at  $y = 1$  has a continuous ramp profile in time given by  $v = (\min(t, 1), 0, 0)^T$ . The simulation is computed on a  $50 \times 50 \times 50$  grid using the  $\mathcal{Q}_3/\mathcal{Q}_2/\text{RT}_1$  discretization. The temporal interval starts from  $t_0 = 0$  up to 50, Alexander's second order strongly S-stable scheme is used with time step size  $\Delta t = 0.005$ .

The flow transitions to a chaotic behaviour at  $t \sim 12$ . Figure 7 shows two snapshots of the flow in the driven cavity. The left part of the figure shows  $\|v\|_2$  together with streamlines of  $v_{\parallel}$  on the plane  $x = 0.5$ . The characteristic corner vortices on this cut through the domain are clearly visible as well as the appearance of the Taylor-Görtler vortices close to  $z = 0.5$ . The right part of the figure shows the  $z$ -component of the vorticity  $\nabla \times v$  on the plane  $z = 0.5$  after the main initial vortex has decayed into several small eddies.

The figure demonstrates in general long time stability of the spatial discretization  $\mathcal{Q}_3/\mathcal{Q}_2/\text{RT}_1$  with  $10^4$  time steps taken.

#### 4.7.2. 3D Taylor-Green vortex

The Taylor-Green vortex has been studied in great detail in [45], C3.5. It aims at testing the accuracy and the performance of high-order methods in the DNS. The initial flow field is given by

$$\begin{aligned}
 v_1(x, y, z, t) &= V_0 \sin\left(\frac{x}{L}\right) \cos\left(\frac{y}{L}\right) \cos\left(\frac{z}{L}\right) \\
 v_2(x, y, z, t) &= -V_0 \cos\left(\frac{x}{L}\right) \sin\left(\frac{y}{L}\right) \cos\left(\frac{z}{L}\right) \\
 v_3(x, y, z, t) &= 0 \\
 p(x, y, z, t) &= p_0 + \frac{\rho_0 V_0^2}{16} \left( \cos\left(\frac{2x}{L}\right) + \cos\left(\frac{2y}{L}\right) \right) \left( \cos\left(\frac{2z}{L}\right) + 2 \right)
 \end{aligned} \tag{44}$$

with periodic boundary conditions in all directions. The general extension of the domain is  $\Omega = (-\pi L, \pi L)^3$  and the Reynolds number is given by  $\text{Re} = \frac{\rho_0 V_0 L}{\mu}$ . As in the references [43, 45] we set  $L = 1$ ,  $V_0 = 1$ ,  $\rho_0 = 1$ ,  $p_0 = 0$ ,  $\text{Re} = 1600$ . In three dimensions the flow transitions to turbulence with development of small scale structures. The simulation is computed on a  $105 \times 105 \times 105$  grid using the  $\mathcal{Q}_3/\mathcal{Q}_2/\text{RT}_1$  discretization which leads to about  $2 \cdot 10^8$  degrees of freedom. The temporal interval starts from  $t_0 = 0$  up to 20, Alexander's second order strongly S-stable scheme is used with time step size  $\Delta t = 0.005$ .

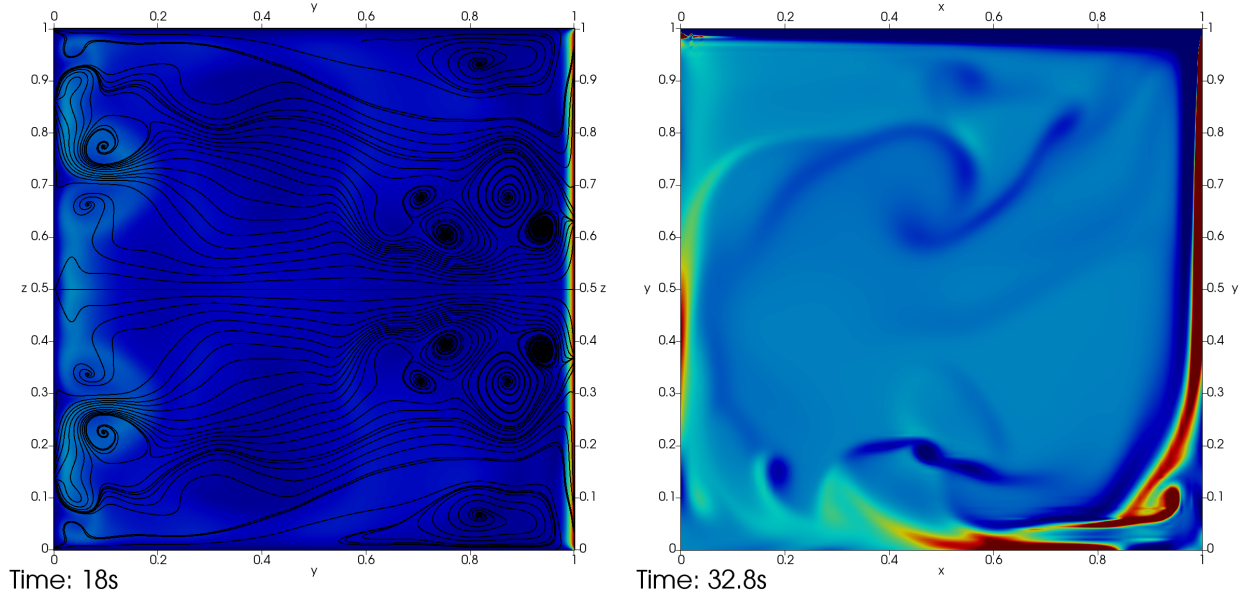


Figure 7: Time-snapshot of  $\|v\|_2$  and streamlines of  $v_{||}$  on plane  $x = 0.5$  (left). Time-snapshot of  $z$ -component of the vorticity  $\nabla \times v$  on plane  $z = 0.5$  (right).

Figure 8 shows the contour surfaces of the  $z$ -component of the vorticity for the values 0.5 in red and -0.5 in blue, respectively, at initial and final condition.

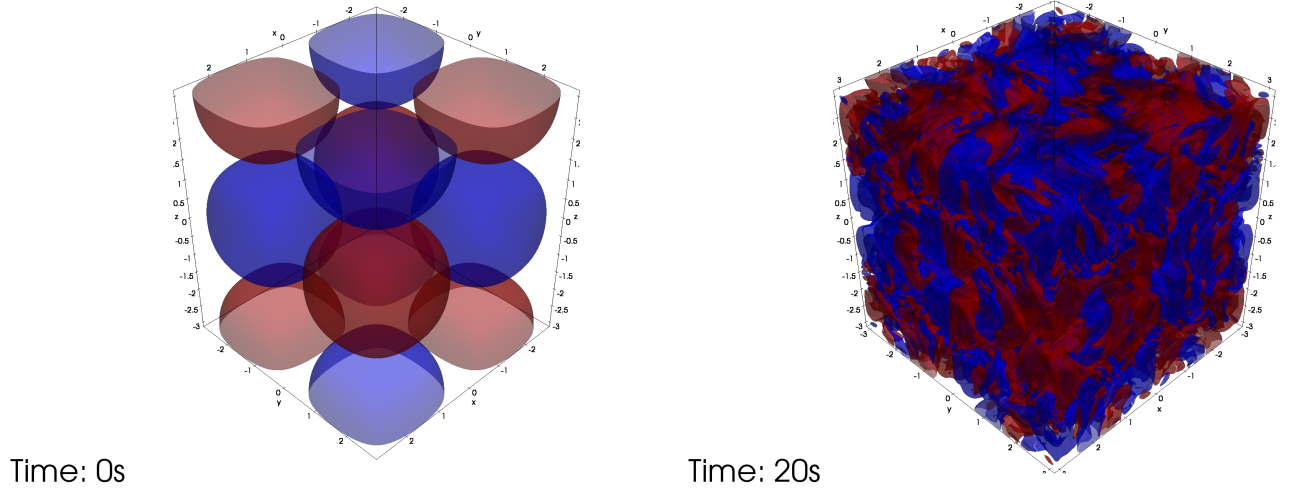


Figure 8: Vorticity visualization for the Taylor-Green vortex problem. The red contours show the levels of the vorticity  $z$ -component with 25 percent of the instantaneous peak. The blue contours show the corresponding negative level.

We now compare our results to the reference values given for this problem that contain the temporal evolution of

- the kinetic energy,  $E_k = \frac{1}{\rho_0|\Omega|} \frac{1}{2}(v, v)_{0,\Omega}$ ,
- the dissipation rate,  $\epsilon = \frac{\nu}{|\Omega|} (\nabla v, \nabla v)_{0,\Omega}$ ,
- the enstrophy,  $\mathcal{E} = \frac{1}{\rho_0|\Omega|} \frac{1}{2}(\nabla \times v, \nabla \times v)_{0,\Omega}$ .

The reference solution was obtained with a dealiased pseudo-spectral code run on a  $512^3$  grid, time integration was performed with a low-storage three-step Runge-Kutta scheme and a time step of  $\Delta t = 10^{-3}$ . The comparison of these three reference quantities is presented in figure 9. Our enstrophy curve is extremely close to the reference curve, furthermore the curves for the kinetic energy and the dissipation rate are indistinguishable with respect to the reference curves.

It can be concluded that the spatial discretization  $Q_3/Q_2/RT_1$  together with the upwind scheme based on the Vijayasundaram flux exhibits long time stability - as in the three-dimensional driven cavity problem - and is good at capturing turbulence accurately.

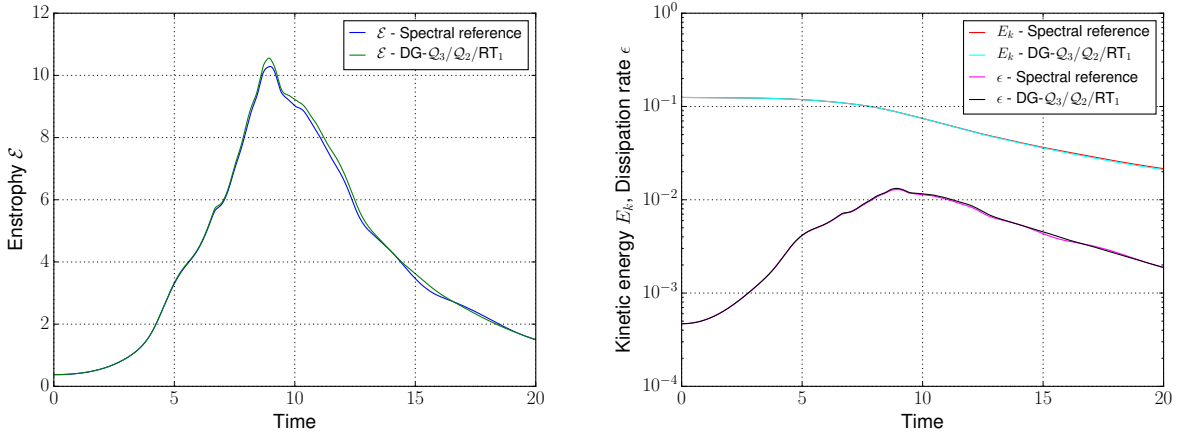


Figure 9: Evolution of the kinetic energy, dissipation rate and enstrophy for the  $Q_3/Q_2/RT_1$  discretization and comparison with the reference values from the spectral code.

## 5. Conclusion and Outlook

In this paper we considered splitting methods, in particular the incremental and rotational incremental pressure correction schemes in combination with a high-order discontinuous Galerkin discretization in space. The momentum equation is solved fully-implicitly with a matrix-free Newton method and sum-factorized element computations to achieve reduced computational complexity at high floating-point performance. The upwind discretization of the convective term in the momentum equation uses a modified Vijayasundaram numerical flux function that takes into account that the discrete velocity field is not in  $H(\text{div})$ . In the Helmholtz projection step we employ an  $H(\text{div})$  postprocessing of the velocity correction which ensures that the projected velocity satisfies the discrete continuity equation. Numerical results confirm that RIPCS is second-order convergent in time for Dirichlet and periodic boundary conditions and has convergence order 1.5 for mixed boundary conditions. Three-dimensional computations with up to  $2 \cdot 10^8$  degrees of freedom and about  $10^4$  time steps show that the scheme is stable for long time computations.

The  $H(\text{div})$  postprocessing in  $RT_k$  spaces is restricted to parallelepiped elements due to the Piola transformation. It remains an open problem how to extend the postprocessing scheme to more general element transformations. In a forthcoming publication we will focus on the performance characteristics and scalability of the parallel implementation.

## Acknowledgements

The first author (M. P.) is supported by a Ph.D. stipend of the Heidelberg Graduate School of Mathematical and Computational Methods for the Sciences (GSC 220). The second author (S. M.) is funded within the DFG special program Software for Exascale Computing (SPP 1648) under contract number Ba 1498/10-2. Computing resources were provided by bwHPC supported by the state of Baden-Württemberg. We would also like to thank Eike Müller for supplying us with a matrix-free block Jacobi and block SOR code for linear equations.

## References

- [1] B. Rivière, V. Girault, Discontinuous finite element methods for incompressible flows on subdomains with non-matching interfaces, *Computer Methods in Applied Mechanics and Engineering* 195 (25–28) (2006) 3274 – 3292, discontinuous Galerkin Methods. doi:<http://dx.doi.org/10.1016/j.cma.2005.06.014>.  
URL <http://www.sciencedirect.com/science/article/pii/S0045782505002690>
- [2] V. Girault, B. Rivière, Mary, F. Wheeler, A discontinuous galerkin method with nonoverlapping domain decomposition for the stokes and navier-stokes problems, *Math. Comp* (2004) 53–84.
- [3] E. Ferrer, R. Willden, A high order discontinuous galerkin finite element solver for the incompressible navier–stokes equations, *Computers & Fluids* 46 (1) (2011) 224 – 230, 10th {ICFD} Conference Series on Numerical Methods for Fluid Dynamics (ICFD 2010). doi:<http://dx.doi.org/10.1016/j.compfluid.2010.10.018>.  
URL <http://www.sciencedirect.com/science/article/pii/S0045793010002860>
- [4] B. Krank, N. Fehn, W. A. Wall, M. Kronbichler, A high-order semi-explicit discontinuous Galerkin solver for 3D incompressible flow with application to DNS and LES of turbulent channel flow, *ArXiv e-prints* arXiv:1607.01323.
- [5] S. Müthing, M. Piatkowski, P. Bastian, High-performance implementation of matrix-free spectral discontinuous galerkin methods, In preparation.
- [6] E. J. Dean, R. Glowinski, On some finite element methods for the numerical simulation of incompressible viscous flow, in: M. D. Gunzburger, R. A. Nicolaides (Eds.), *Incompressible Computational Fluid Dynamics*, Cambridge University Press, 1993, pp. 17–66, cambridge Books Online.  
URL <http://dx.doi.org/10.1017/CB09780511574856.003>
- [7] H. C. Elman, D. J. Silvester, A. J. Wathen, *Finite elements and fast iterative solvers: with applications in incompressible fluid dynamics*, Oxford University Press, 2014, second edition.
- [8] A. J. Chorin, Numerical solution of the navier-stokes equations, *Mathematics of Computation* 22 (104) (1968) 745–762.  
URL <http://www.jstor.org/stable/2004575>
- [9] R. Témam, Sur l’approximation de la solution des équations de navier-stokes par la méthode des pas fractionnaires (ii), *Archive for Rational Mechanics and Analysis* 33 (5) (1969) 377–385. doi:10.1007/BF00247696.  
URL <http://dx.doi.org/10.1007/BF00247696>
- [10] R. Rannacher, On chorin’s projection method for the incompressible navier-stokes equations, *Springer Berlin Heidelberg, Berlin, Heidelberg*, 1992, pp. 167–183. doi:10.1007/BFb0090341.  
URL <http://dx.doi.org/10.1007/BFb0090341>
- [11] W. E, J.-G. Liu, Projection method i: Convergence and numerical boundary layers, *SIAM Journal on Numerical Analysis* 32 (4) (1995) 1017–1057. doi:10.1137/0732047.
- [12] W. E, J.-G. Liu, Projection method ii: Godunov–ryabenki analysis, *SIAM Journal on Numerical Analysis* 33 (4) (1996) 1597–1621. doi:10.1137/S003614299426450X.
- [13] G. E. Karniadakis, M. Israeli, S. A. Orszag, High-order splitting methods for the incompressible navier-stokes equations, *Journal of Computational Physics* 97 (2) (1991) 414 – 443. doi:[http://dx.doi.org/10.1016/0021-9991\(91\)90007-8](http://dx.doi.org/10.1016/0021-9991(91)90007-8).  
URL <http://www.sciencedirect.com/science/article/pii/0021999191900078>
- [14] L. J. P. Timmermans, P. D. Mineev, F. N. Van De Vosse, An approximate projection scheme for incompressible flow using spectral elements, *International Journal for Numerical Methods in Fluids* 22 (7) (1996) 673–688.
- [15] J. L. Guermond, J. Shen, A new class of truly consistent splitting schemes for incompressible flows, *J. Comput. Phys.* 192 (2003) 262–276.
- [16] J. L. Guermond, J. Shen, On the error estimates of rotational pressure-correction projection methods, *Math. Comp* 73 (2004) 1719–1737.
- [17] G. Karniadakis, S. Sherwin, *Spectral/hp Element Methods for Computational Fluid Dynamics*, Oxford University Press, 2005.
- [18] J. L. Guermond, P. Mineev, J. Shen, An overview of projection methods for incompressible flows, *Computer Methods in Applied Mechanics and Engineering* 195 (2006) 6011–6045.
- [19] K. Goda, A multistep technique with implicit difference schemes for calculating two- or three-dimensional cavity flows, *Journal of Computational Physics* 30 (1) (1979) 76 – 95. doi:[http://dx.doi.org/10.1016/0021-9991\(79\)90088-3](http://dx.doi.org/10.1016/0021-9991(79)90088-3).  
URL <http://www.sciencedirect.com/science/article/pii/0021999179900883>
- [20] D. Steinmoeller, M. Stastna, K. Lamb, A short note on the discontinuous galerkin discretization of the pressure projection operator in incompressible flow, *Journal of Computational Physics* 251 (2013) 480 – 486. doi:<http://dx.doi.org/10.1016/j.jcp.2013.05.036>.  
URL <http://www.sciencedirect.com/science/article/pii/S0021999113004026>

- [21] S. M. Joshi, P. J. Diamessis, D. T. Steinmoeller, M. Stastna, G. N. Thomsen, A post-processing technique for stabilizing the discontinuous pressure projection operator in marginally-resolved incompressible inviscid flow, *Computers & Fluids* 139 (2016) 120 – 129, 13th {USNCCM} International Symposium of High-Order Methods for Computational Fluid Dynamics - A special issue dedicated to the 60th birthday of Professor David Kopriva. doi:<http://dx.doi.org/10.1016/j.compfluid.2016.04.021>.  
URL <http://www.sciencedirect.com/science/article/pii/S0045793016301311>
- [22] P. Bastian, B. Rivière, Superconvergence and h(div) projection for discontinuous galerkin methods, *International Journal for Numerical Methods in Fluids* 42 (10) (2003) 1043–1057. doi:10.1002/flid.562.  
URL <http://dx.doi.org/10.1002/flid.562>
- [23] A. Ern, S. Nicaise, M. Vohralík, An accurate H(div) flux reconstruction for discontinuous Galerkin approximations of elliptic problems, *Comptes Rendus Mathématique* 345 (12) (2007) 709 – 712. doi:<http://dx.doi.org/10.1016/j.crma.2007.10.036>.  
URL <http://www.sciencedirect.com/science/article/pii/S1631073X07004360>
- [24] J. L. Guermond, P. Mineev, J. Shen, Error analysis of pressure-correction schemes for the time-dependent stokes equations with open boundary conditions, *SIAM Journal on Numerical Analysis* 43 (1) (2005) 239–258. arXiv:<http://dx.doi.org/10.1137/040604418>, doi:10.1137/040604418.  
URL <http://dx.doi.org/10.1137/040604418>
- [25] V. Girault, P. Raviart, *Finite Element Methods for the Navier-Stokes Equations*, Springer, 1986.
- [26] R. Témam, *Navier-Stokes Equations. Theory and numerical analysis*, North Holland, Amsterdam, 1987.
- [27] P. Houston, R. Hartmann, An optimal order interior penalty discontinuous Galerkin discretization of the compressible Navier-Stokes equations, *J. Comp. Phys.* 227 (2008) 9670–9685.
- [28] P. Bastian, M. Blatt, R. Scheichl, Algebraic multigrid for discontinuous Galerkin discretizations, *Numer. Linear Algebra Appl.* 19 (2) (2012) 367–388. doi:10.1002/nla.1816.
- [29] M. Feistauer, J. Felcman, I. Straskraba, *Mathematical and Computational Methods for Compressible Flow*, Clarendon Press, 2003.
- [30] V. Dolejší, M. Feistauer, A semi-implicit discontinuous galerkin finite element method for the numerical solution of inviscid compressible flow, *Journal of Computational Physics* 198 (2) (2004) 727 – 746. doi:<http://dx.doi.org/10.1016/j.jcp.2004.01.023>.  
URL <http://www.sciencedirect.com/science/article/pii/S0021999104000609>
- [31] L. Evans, *Partial Differential Equations*, 2nd Edition, American Mathematical Society, 2010.
- [32] J.-L. G. a. Alexandre Ern, *Theory and Practice of Finite Elements*, 1st Edition, Applied Mathematical Sciences 159, Springer-Verlag New York, 2004.
- [33] B. Schweizer, *Partielle Differentialgleichungen, Eine anwendungsorientierte Einführung*, Springer-Verlag, 2013.
- [34] H. Bhatia, G. Norgard, V. Pascucci, P.-T. Bremer, The helmholtz-hodge decomposition&#x2014;a survey, *IEEE Transactions on Visualization and Computer Graphics* 19 (8) (2013) 1386–1404. doi:10.1109/TVCG.2012.316.  
URL <http://dx.doi.org/10.1109/TVCG.2012.316>
- [35] F. Brezzi, M. Fortin, *Mixed and Hybrid Finite Element Methods*, Springer-Verlag, 1991.
- [36] R. Alexander, Diagonally implicit Runge–Kutta methods for stiff O.D.E.’s, *SIAM Journal on Numerical Analysis* 14 (6) (1977) 1006–1021.
- [37] P. Bastian, M. Blatt, A. Dedner, C. Engwer, R. Klöforn, M. Ohlberger, O. Sander, A generic grid interface for parallel and adaptive scientific computing. Part I: Abstract framework, *Computing* 82 (2–3) (2008) 103–119. doi:10.1007/s00607-008-0003-x.
- [38] P. Bastian, C. Engwer, J. Fahlke, M. Geveler, D. Göddeke, O. Iliev, O. Ippisch, R. Milk, J. Mohring, S. Müthing, M. Ohlberger, D. Ribbrock, S. Turek, *Hardware-Based Efficiency Advances in the EXA-DUNE Project*, Springer International Publishing, Cham, 2016, p. 3–23. doi:10.1007/978-3-319-40528-5\_1.  
URL [http://dx.doi.org/10.1007/978-3-319-40528-5\\_1](http://dx.doi.org/10.1007/978-3-319-40528-5_1)
- [39] E. Müller, M. Piatkowski, S. Müthing, R. Scheichl, P. Bastian, Matrix-free preconditioners, In preparation.
- [40] A. E. G. G. I. Taylor, Mechanism of the production of small eddies from large ones, *Proceedings of the Royal Society of London. Series A, Mathematical and Physical Sciences* 158 (895) (1937) 499–521.  
URL <http://www.jstor.org/stable/96892>
- [41] P. Rabenold, E. Balaras, Parallel adaptive mesh refinement for the incompressible navier-stokes equations.
- [42] C. R. Ethier, D. A. Steinmann, Exact fully 3D Navier–Stokes solution for benchmarking, *Internat. J. Numer. Methods Fluids* 19 (1994) 369 – 375.
- [43] A. Logg, K.-A. Mardal, G. N. Wells (Eds.), *Automated Solution of Differential Equations by the Finite Element Method*, Vol. 84 of *Lecture Notes in Computational Science and Engineering*, Springer, 2012. doi:10.1007/978-3-642-23099-8.  
URL <http://dx.doi.org/10.1007/978-3-642-23099-8>
- [44] R. Iwatsu, K. Ishii, T. Kawamura, K. Kuwahara, J. M. Hyun, Numerical simulation of three-dimensional flow structure in a driven cavity, *Fluid Dynamics Research* 5 (3) (1989) 173.  
URL <http://stacks.iop.org/1873-7005/5/i=3/a=A03>
- [45] 2nd international workshop on high-order cfd methods, cologne, germany (May 2013).  
URL <http://www.dlr.de/as/hicofd>